J. Fluid Mech. (2019), *vol.* 881, *pp.* 815–858. © Cambridge University Press 2019
doi:10.1017/jfm.2019.738

Mapping the properties of the vortex-induced vibrations of flexible cylinders in uniform oncoming flow

Dixia Fan[1], **Zhicheng Wang**[1,†], **Michael S. Triantafyllou**[1] and **George Em Karniadakis**[2]

[1]Department of Mechanical Engineering, Massachusetts Institute Technology, Cambridge, MA 02139, USA

[2]Division of Applied Mathematics, Brown University, Providence, RI 02912, USA

(Received 9 March 2019; revised 7 July 2019; accepted 2 September 2019;
first published online 25 October 2019)

Flexible structures placed within an oncoming flow exhibit far more complex vortex-induced dynamics than flexibly mounted rigid cylinders, because they involve the distributed interaction between the structural and wake dynamics along the entire span. Hence, mapping the well-understood properties of rigid cylinder vibrations to those of strings and beams has been elusive. We show here with a combination of experiments, conducted at Reynolds number, *Re* from 250 to 2300, and computational fluid dynamics that such a mapping is possible for flexible structures in uniform flow undergoing combined cross-flow and in-line oscillations, but only when additional concepts are introduced to model the extended coupling of the flow and the structure. The in-line response consists of largely standing waves that define cells, each cell spanning the distance between adjacent nodes, over which stable vortical patterns form, whose features (‘2S’ versus ‘P+S’) depend strongly on the true reduced velocity, $V_r = U/f_y d$, where U is the inflow velocity, f_y is the cross-flow vibration frequency and d is the cylinder diameter, and the phase angle between in-line and cross-flow response; while the cross-flow response may contain travelling waves, breaking the symmetry of the problem. The axial distribution of the highly variable effective added masses in the cross-flow and in-line directions, and the local phase angle between in-line and cross-flow motion determine the single frequency of cross-flow response, while the in-line response vibrates at twice the cross-flow frequency. The cross-flow and in-line lift coefficients in phase with velocity depend strongly on the true reduced velocity but also on the local phase angle between in-line and cross-flow motions. Modal shapes can be defined for in-line and cross-flow, based on the resemblance of the response to conventional modes, which can be in the ratio of either ‘$2n/n$’ or ‘$(2n-1)/n$’, where n is the order of the cross-flow response mode. We use an underwater optical tracking system to reconstruct the sectional fluid forces in a flexible structure and show that, once the cross-flow and in-line motion features are known, employing strip theory and the hydrodynamic coefficients obtained from forced rigid cylinder experiments allows us to predict the distributed forces accurately.

Key words: flow–structure interactions, vortex dynamics

---

† Email address for correspondence: zhicheng@mit.edu

1. Introduction

The prediction of the vortex-induced vibrations (VIV) of long flexible structures is a challenging problem and it is encountered in a wide range of engineering applications, such as hanging electric wires vibrating in the wind, and marine risers and cables oscillating within ocean current. Vortex-induced vibrations may result in severe fatigue damage (Zheng *et al.* 2014*b*), hence a large amount of research has focused on better understanding and predicting the flexible cylinder VIV response, as well devising suppression methods to mitigate excessive fatigue damage (Fan & Triantafyllou 2017).

For a stationary circular cylinder with uniform cross-section placed in uniform flow, unsteady cross-flow (CF) and in-line (IL), hydrodynamic forces (Bishop & Hassan 1964) develop due to the shedding of alternating sign vortices in the wake of the cylinder (Williamson 1996). In what has become a canonical fluid-structure interaction problem, the cylinder is flexibly mounted and is allowed to vibrate in the CF direction. A large number of publications have been devoted to understanding the principal mechanisms of flow instability and flow-structure interaction that lead to such vibrations (Williamson & Govardhan 2004; Gabbai & Benaroya 2005; Williamson & Govardhan 2008; Bearman 2011; Raghavan & Bernitsas 2011). It has been established that over a broad range of incoming velocities, different regimes of response can be classified as initial, upper and lower branches (Khalak & Williamson 1999), and distinct vortex shedding modes were identified (Williamson & Roshko 1988; Govardhan & Williamson 2000). An important concept of the flexibly mounted rigid cylinder VIV is that of ‘lock-in’ (Bearman 1984), wherein the vortex shedding frequency is entrained to coincide with the CF vibration frequency. During ‘lock-in’, moderate response amplitudes, typically self-limited to approximately one diameter, and a wide range of synchronization frequencies have been observed. The vortex shedding frequency can differ from the Strouhal frequency of a fixed cylinder, because, as work via flow visualization has revealed, the relative motion between the vibrating cylinder and the shed vortices can significantly alter the effective fluid added mass (Sarpkaya 2004), resulting in a variable natural frequency as a function of stream velocity (Williamson 1996).

Significant variations of the fluid forces as a function of the oncoming stream velocity have been found for a cylinder oscillating in the CF direction, due to changes in the vortex shedding pattern. Therefore, experiments were conducted, where a rigid cylinder was forced to vibrate in the CF direction at prescribed frequencies and amplitudes (Sarpkaya 1978). In particular, studies focused on the mean drag coefficient C_d, the lift coefficient in-phase with the velocity C_{lv} and the added mass coefficient in the CF direction C_{my}, calculated from the component of the lift force in-phase with acceleration (Staubli 1983; Gopalkrishnan 1993; Sarpkaya 1995). A comprehensive set of experiments was performed at the MIT tow tank facility by Gopalkrishnan (1993) by varying systematically the true reduced velocity $V_r = U/fd$ and non-dimensional CF amplitude A_y/d, where U is the prescribed fluid velocity, f the prescribed motion frequency, A_y the prescribed motion amplitude and d the cylinder model diameter. The experiments showed that regions of positive C_{lv}, denoting net energy transferred from the fluid to the structure over one motion period, were located in a certain range of V_r and A_y/d. In addition, it was found that the added mass coefficient could vary significantly from a negative value to a large positive value around the true reduced velocity $V_r = 5.9$. These measured hydrodynamic coefficients resulted in an accurate prediction of the rigid cylinder VIV in the CF direction (Wang, So & Chan 2003), and they have served as databases for fluid forces in semi-empirical flexible riser VIV prediction codes (Triantafyllou *et al.* 1999; Larsen *et al.* 2001; Roveri & Vandiver 2001).

However, considerable differences were found in both structural responses as well as wake patterns, if the cylinder was allowed to move in combined IL and CF response (Aronsen 2007). It was found that IL motion would affect the CF vibration substantially, even though the IL motion is usually 2–6 times smaller than the CF motion. For low mass ratio cases, the cylinder reached larger CF amplitudes, up to 1.5d (Jauvtis & Williamson 2003) and a wider synchronization frequency range versus U_r in the CF direction (Dahl 2008). Furthermore, some new vortex shedding patterns, such as a '2T' mode, were identified (Jauvtis & Williamson 2004). For a rigid cylinder VIV with coupled IL and CF motions, the phase θ between the IL and the CF motions was found to have a strong influence on the fluid forces on the oscillating cylinder (Jauvtis & Williamson 2004). Forced vibration cylinder experiments (Dahl *et al.* 2007, 2010) revealed that positive energy-in, *viz.* positive C_{lv}, was strongly associated with a phase angle θ corresponding to a counter-clockwise trajectory. The occurrence of high harmonics (3rd and *t*th harmonics) in the lift force was also found to be correlated with specific values of θ (Dahl, Hover & Triantafyllou 2008).

Fewer experimental studies have been performed on long flexible cylinder VIV. Brika & Laneville (1993) conducted experiments on a flexible cylinder placed in uniform flow. The first mode of vibration was excited in the CF direction, and the amplitude response and the vortex wake were found to resemble those found in the rigid cylinder case. In experiments performed by Huera-Huarte & Bearman (2009*a*,*b*), both the IL and the CF motions were reported to be well synchronized with the wake, and a steady phase between the IL and the CF trajectories was observed, associated with different vortex modes along the span. Vandiver *et al.* (2006) and Vandiver, Jaiswal & Jhingran (2009) performed field tests by towing flexible cylinders within the Gulf Stream, exciting high mode vibrations with mixed patterns of standing and travelling waves. Through analysis of the 'Norwegian deepwater programme riser high mode VIV tests', (Braaten & Lie 2004; Modarres-Sadeghi *et al.* 2010, 2011) established that a 38 m long flexible riser model exhibits chaotic response, switching randomly between steady-state and chaotic states, with strong high harmonic components in the lift force during steady-state response. Chaplin *et al.* (2005*b*) conducted experiments on a flexible cylinder in a stepped incoming flow. The authors reported the amplitude and frequency response over a wide range of incoming velocities, highlighting multiple modes excited in both the IL and the CF directions. The results were used to compare the results from different numerical and semi-empirical codes (Chaplin *et al.* 2005*a*). The predictions, although capturing some flexible cylinder VIV features, also showed discrepancies from the experiments.

A key factor for better prediction of flexible cylinder VIV is the measurement of the hydrodynamic coefficients as distributed along the span. Inverse methods were employed to identify the fluid force distribution by Huera-Huarte, Bearman & Chaplin (2006), who applied a finite element method to reconstruct the fluid forces of a flexible cylinder from its vibration responses; and by Tang *et al.* (2011) who developed a master–slave technique to reduce the rotational degrees of freedom in fluid force reconstruction. Wu (2011) developed new schemes integrating least-squares and Kalman filter techniques and showed that the hydrodynamic coefficients along the flexible cylinder were affected by the values of the phase angle θ. Han *et al.* (2018) used a similar least-squares method to investigate the fluid forces on a flexible cylinder placed at a large inclination angle relative to a uniform incoming flow. A basic conclusion of the experimental results is that the local hydrodynamic

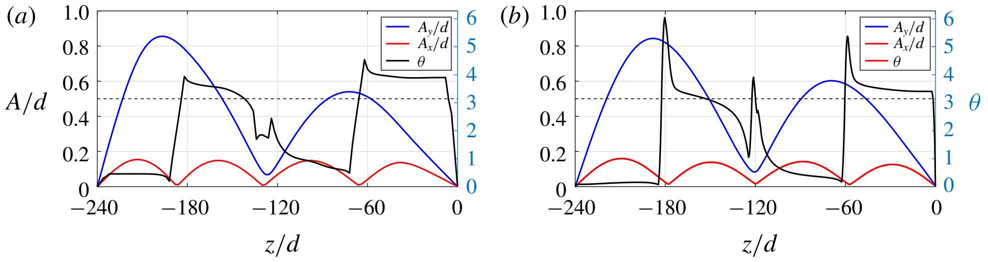

Experiment

Simulation

FIGURE 1. (Colour online) Comparison between experimental measurements and simulation results at $U_r = 12.66$. The black dashed line denotes $\theta = \pi$ (where $\theta \in [0, \pi]$ represents counter-clockwise cross-flow and in-line trajectory, and $\theta \in [\pi, 2\pi]$ represents clockwise cross-flow and in-line trajectory). Note that in the simulation, the tension is uniform along the cylinder, while it is linearly distributed in the experiment, where the tension at one end is 33 % larger than that at the other end.

coefficients of a flexible cylinder are qualitatively different from those for a rigid cylinder undergoing CF oscillations.

There is a large number of published computational studies on flexible cylinder VIV. Some works represented empirically the effect of the oncoming flow through distributed wake oscillators along the flexible cylinder (Facchinetti, De Langre & Biolley 2004; Violette, De Langre & Szydlowski 2007), with qualitative agreement with experimental and direct numerical simulation (DNS) results. High fidelity DNS using the spectral-element method were presented in Newman & Karniadakis (1997) and Evangelinos & Karniadakis (1999) for a uniform flexible cylinder with an aspect ratio of 4π in uniform flow at Reynolds numbers 100, 200 and 1000. Structural response and force distribution were reported by Newman & Karniadakis (1996) and Evangelinos, Lucor & Karniadakis (2000) in order to establish a connection between the flexible cylinder free vibration and the rigid cylinder forced vibration. More recently, Bourguet *et al.* (2011) numerically confirmed that, similar to forced rigid cylinder vibration, θ values corresponding to counter-clockwise trajectories are favourable to positive energy transfer from fluid to structure. However, to the best of our knowledge, there is no direct comparison between numerical simulation and experimental measurements for long flexible cylinders undergoing VIV.

In this paper, we investigate a tension-dominated flexible cylinder of aspect ratio of 240, moderate mass ratio of 4.0, and pinned at both ends both experimentally and through simulation. Very good agreement between the experimental results and the simulation results was obtained as can be seen in figure 1, where the results of the CF amplitude A_y/d (blue line), the IL amplitude A_x/d (red line) and the phase θ distribution (black line) are displayed side by side. The paper is organized as follows. Section 2 presents the experimental and numerical methods. Section 3 discusses the experimental results with an emphasis on the connection between a rigid cylinder and a flexible cylinder. Section 4 provides the numerical simulation results of the flexible cylinder wake patterns. Section 5 summarizes the main findings of the paper. In the appendices, we describe the method we used to acquire sectional hydrodynamic coefficients from the measured motion data; we provide a sample of the hydrodynamic coefficients measured from the rigid cylinder forced vibration experiment as well as a comparison between our experimental and simulation results.

2. Experimental and numerical method description

2.1. *Experimental method and model*

The uniform flexible cylinder model has a diameter $d = 0.5$ cm and a length $L = 120$ cm, with a resulting aspect ratio of 240. The model is constructed/moulded via urethane rubber (density of 1.38 g cm^{-3}) mixed with tungsten (density of 19.3 g cm^{-3}) powder in order to reach a mass ratio of $m^* = 4.0$ (the ratio between structural mass to displaced fluid mass). In addition, a fishing line is embedded in the centre during the moulding process to provide sufficient axial stiffness. In the current experiment, the effect of the bending stiffness on the model's natural frequency and modal shape is negligible, compared to that of the tensions applied. Note that the structural damping of the urethane rubber material is higher than the traditional metal or ABS plastic cylinder model. Nonetheless, the damping ratio of the current flexible model is 8.7 %, as obtained from the pluck test in the air.

We performed systematic experiments at the MIT tow tank facility with a water depth of 1.22 m. An aluminium frame was built to provide mounting points for the bottom of the model and a '6-axis ATI Gamma' sensor was installed on top of the frame in order to measure the model's top tension in each experimental run. The vertically installed model had a 97 % total immersion length, and it was clamped at both ends. The model was towed to generate a uniform inflow with different speeds from 0.05 to 0.46 m s^{-1}, achieving Reynolds numbers Re from 250 to 2300 while the reduced velocity varied from 4.8 to 36. Here, the reduced velocity U_r and the true reduced velocity V_r are defined as follows:

$$\left.\begin{aligned} U_r &= \frac{U}{f_{n1} d}, \\ V_r &= \frac{U}{f_y d}, \end{aligned}\right\} \tag{2.1}$$

where U is the inflow velocity, d is the model diameter, f_{n1} is the first modal natural frequency, calculated based on the measured tension, assuming $C_m = 1.0$ along the model, and f_y is the actual vibration frequency measured in the CF direction. Figure 2 shows a sketch of the experimental set-up, while table 1 lists the experimental parameters.

We applied our newly developed underwater optical methods using eight high-speed cameras to capture the IL and CF vibrations for a total of 52 locations (staggered black and white markers) along the model. Compared to the traditional strain-gauge and accelerometer measurement for flexible cylinder VIV experiments, the optical tracking system provides both temporally and spatially dense and direct measurements on the model displacement response (Fan, Du & Triantafyllou 2016). Three cameras are installed over $160d$ downstream of the model to measure the CF vibration while five cameras are installed $100d$ besides the model to measure the IL vibration. At the same time, four 1500-lumen underwater lights were installed to provide enough camera background lighting. Corresponding image processing and motion tracking code were developed to capture and follow the trajectory of either white or black markers (Fan & Triantafyllou 2017). Figure 2(*b*) displays a sample frame of the raw and processed images for one of the cameras. More details about the camera set-up and the image process method are described in appendix A.

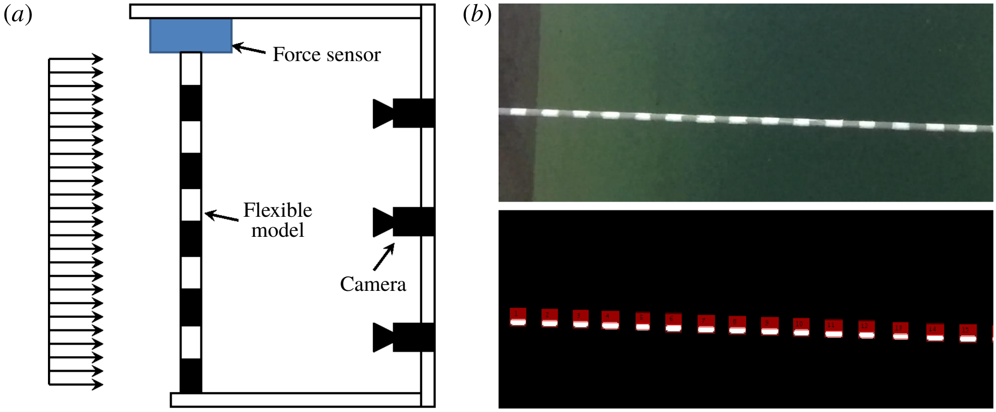

FIGURE 2. (Colour online) The flexible model in the MIT tow tank: (*a*) a sketch of the experimental set-up that shows the uniform incoming flow and the black and white strips used for motion tracking purposes; (*b*) sample raw (top) and processed (bottom) image shows that the red bounding box captures the motion of the white markers.

2.2. *Numerical method and model*

In order to obtain a quantitative understanding of the complex vortex shedding process, we carried out a large-eddy simulation (LES) study by using the entropy-viscosity method, which was proposed by Guermond, Pasquetti & Popov (2011*a*,*b*) and later developed further for complex flows in Wang *et al.* (2018, 2019). In the simulation, the governing equations of the incompressible flow are solved by a Fourier/spectral-element code that employs spectral-element discretization in the (x–y) plane and Fourier expansion along the riser axial direction (z) as presented in Karniadakis & Sherwin (2005). The coordinate transformation method proposed in Newman & Karniadakis (1997) is employed to deal with the boundary deformation due to the vibration. On the (x–y) plane, the computational domain has a size of $[-6.5d, 23.5d] \times [-20d, 20d]$, which is partitioned into 2 616 quadrilateral elements, where $d = 1$ is the cylinder diameter whose centre is placed at (0, 0). On the left boundary of the domain where $x/d = -6.5$, $u = U$, $v = 0$, $w = 0$ are imposed, where u, v, w are the three components of velocity vector $\boldsymbol{u}$; on the right boundary where $x/d = 23.5$, $p = 0$ and $\partial \boldsymbol{u}/\partial \boldsymbol{n} = 0$ are prescribed, where p is the pressure and $\boldsymbol{n}$ is the normal vector; on both top and bottom boundaries where $y/d = \pm 20$, a periodic boundary condition is used.

The cylinder motion is governed by a linear beam-string equation as follows:

$$\frac{\partial^2 \xi_J}{\partial t^2} + 2\zeta \omega_n \frac{\partial \xi_J}{\partial t} + \frac{EI}{\mu}\frac{\partial^4 \xi_J}{\partial z^4} - \frac{T}{\mu}\frac{\partial^2 \xi_J}{\partial z^2} = \frac{F}{\mu}, \tag{2.2}$$

where ξ_J is the displacement in the J direction ($J = x$ or $J = y$), μ is the cylinder mass per unit length, the damping coefficient $\zeta = 8.7\,\%$ is equal to that of experiment with $\omega_n = 2\pi f_{n1}$, T is the tension and EI is the bending stiffness. The above equation is constrained by pinned boundary conditions ($\xi_J = 0$ and $\partial^2 \xi_J/\partial z^2 = 0$) at both ends. Note that in the simulation, $T = (UL/U_r d)^2(4\mu + C_m \rho \pi d^2)$ with $C_m = 1.0$, where U_r is the corresponding reduced velocity defined in equation (2.1), while the value of EI is set as small as $0.02T$, in order to mimic a tension dominated riser (see Evangelinos

Model parameters	Values
Diameter d	0.5 cm
Length L	120 cm
Aspect ratio L/d	240
Immersed ratio	97 %
Mass per unit length μ	0.0785 kg m^{-1}
Mass ratio m^*	4.0
Damping ratio ζ	8.7 %
Bending stiffness EI	0.000245 Nm^2
Experimental runs	
Towing velocity	0.05–0.46 m s^{-1}
Reynolds number Re	250–2300
Reduced velocity U_r	4.8–36

TABLE 1. Values of the experimental parameters of the uniform flexible model.

& Karniadakis 1999). F is the J-component of the hydrodynamic force exerted on the cylinder surface, computed from the integral of the pressure and viscous stress terms using the following equation:

$$F = \oint (-p\boldsymbol{n} + \nu(\nabla \boldsymbol{u} + \nabla \boldsymbol{u}^T) \cdot \boldsymbol{n}), \tag{2.3}$$

where the integration is performed around the circumference of the circular cross-section and $\boldsymbol{n}$ is the outward unit normal on the cylinder, ν is the kinematic viscosity. In order to solve the governing equation (2.2), we have used the second-order central-difference scheme in space and the Runge–Kutta method in time. For all the simulations in this paper, unless mentioned explicitly, a cubic polynomial is used in each element per direction and 512 Fourier planes are used along the axis (z-direction). For each simulation, the total computational time $tU_\infty/d \geqslant 500$ with a time step $\Delta t = 1.5 \times 10^{-3}$. In total, eight simulations using the same parameters as those of the experiments with Ur in the range of [10.75, 17.22] were performed. Validation tests on displacements and excited frequencies are presented in appendix E.

3. Structural response and fluid forces of the vibrating flexible cylinder: experimental results and discussion

In this section, we first present the frequency and displacement response in the experiment with an emphasis on the discontinuous displacement response during the modal group switch. Subsequently, the result of the inverse hydrodynamic coefficients distribution along the flexible model is reconstructed at each cross-section and compared directly with the prediction from the combined CF and IL forced vibration experiment on rigid cylinders. The newly constructed hydrodynamic database is an extension from the previous experiments by Dahl *et al.* (2010) and Zheng *et al.* (2014*a*). Despite the Re difference between the rigid and flexible cylinder experiments, we find a good agreement between the two cases. We then pay special attention to what happens to the lift coefficient in-phase with the velocity and added mass coefficient distribution along the span. Moreover, we document that the θ distribution along the flexible model is a critical factor in determining the

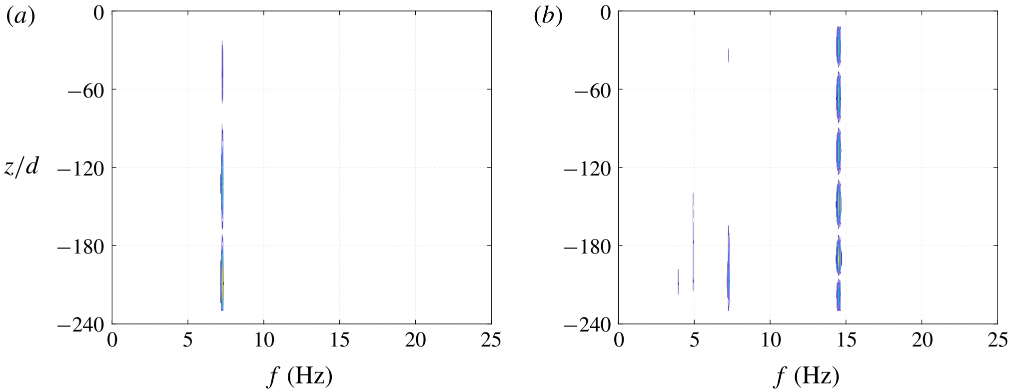

FIGURE 3. (Colour online) Frequency response along the flexible model at $U = 0.19\ \mathrm{m\ s^{-1}}$ ($U_r = 18.1$): (*a*) in the CF direction, the model vibrates within a narrow-band single frequency, and the inset figure plots the CF frequency response at $z/d = -160$; (*b*) in the IL direction, the 2nd harmonic of the vibration dominates the response.

hydrodynamic coefficient distribution and its variation in and between the different modal groups.

3.1. *Frequency and displacement response*

In figure 3(*a*), we plot the VIV frequency response of the flexible cylinder at $U = 0.19\ \mathrm{m\ s^{-1}}$ ($Ur = 18.1$). The flexible model vibrates in the CF direction at one single narrow-banded frequency along the entire span. We also see in figure 3(*b*) that the exact 2nd harmonic vibration dominates the entire model although some low-frequency responses can be spotted in the IL direction. Such vibration patterns of the single narrow-band frequency response in the CF direction and the dominating 2nd harmonic vibration in the IL direction were found consistent in the current experiment.

Based on the dominant frequency components from the power spectral density (PSD), the corresponding 1/10th highest peak of the IL and the CF displacement along the model is plotted in figures 4(*a*) and 5(*a*) against U_r. With increasing U_r, higher modes are excited in both the IL and the CF directions. In the current experiment, the 1st to 6th CF modes and the 2nd to 11th IL modes are excited. In general, in the CF direction, the results show on average 5–6 times larger displacement response than that in the IL direction.

Furthermore, three different cases of U_r ($U_r = 12.7$, $U_r = 21.6$ and $U_r = 32.2$) are selected to plot the displacement response along the entire model in figure 4(*b*) for the CF response and figure 5(*b*) for the IL response. We observe an asymmetric modal displacement response along the span in the CF direction, while in the IL direction, a symmetric sinusoidal mode shape is consistently found. A comparison between the case of $U_r = 12.7$ and the case of $U_r = 32.2$ shows that at lower U_r, a pure standing wave is observed in the CF direction. In contrast, with the increasing U_r, a mixture of standing and travelling wave response gradually appears in the CF direction. As shown in figure 4, the CF displacement response is rather 'flat' and no clear node can be easily identified. However, in the IL direction, the model displays a pure standing wave pattern at both low and high U_r. In addition, figures 4(*c*) and 5(*c*) plot the CF and the IL displacements as a function of U_r at three different locations ($z/d = -168$,

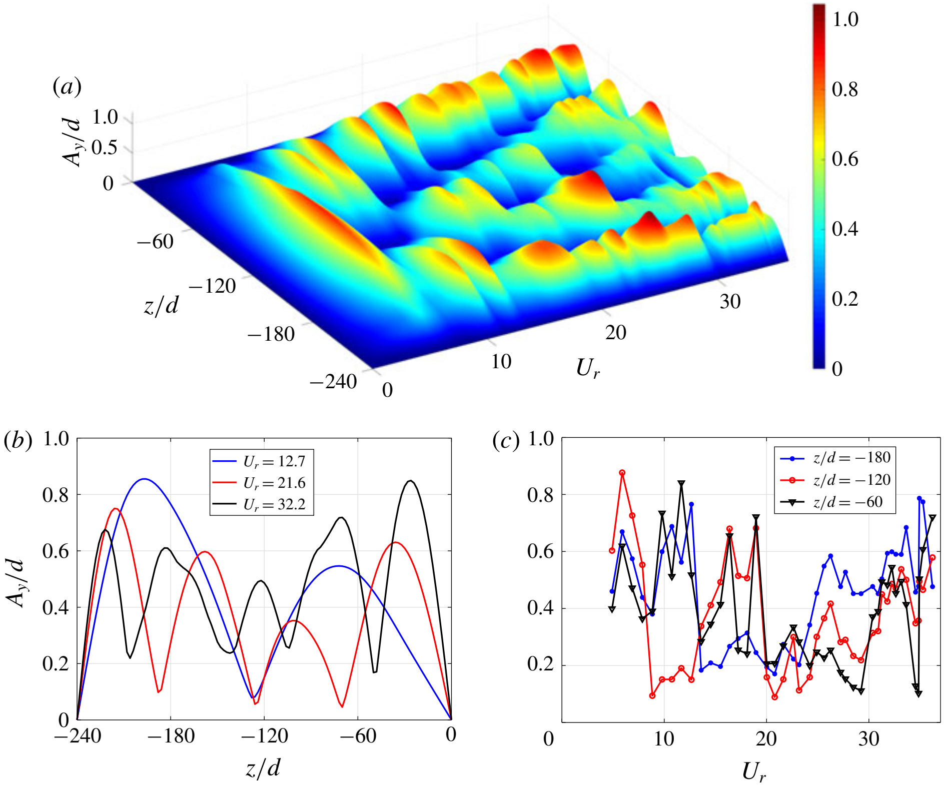

FIGURE 4. (Colour online) Experimental results of the displacement response in the CF direction: (*a*) three-dimensional (3-D) visualization of the displacement response as a function of z/d and U_r; (*b*) displacement response along the flexible model at $U_r = 12.7$, 21.6 and 32.2; (*c*) displacement response versus U_r at locations $z/d = -180$, -120 and -60. Note that the displacement response here is presented based on 1/10th highest peak measurement. In the current experiment, as U_r increases, the flexible model vibrates at a higher mode number up to 6th mode in the CF direction. The amplitude response along the model span at higher U_r is asymmetric, a sign of mixed standing and travelling wave response patterns.

$z/d = -108$ and $z/d = -48$) along the model, respectively. At these three locations, both the IL and the CF displacements vary significantly with U_r.

From figures 4(*a*) and 5(*a*), the maximum amplitudes of the IL and the CF displacement response across the span for each U_r are selected and plotted in figures 6 and 7, together with the response frequency ratio in either the IL or the CF direction. The response frequency ratio is defined here as the ratio between the response frequency and the model's first modal natural frequency predicted in still water.

In figures 6 and 7, we first observe that the mode number of the IL and the CF displacement responses increase with U_r. We then group all experimental cases of U_r with the same modal group (the modal group is defined as the model displacement response at the same modes in both the IL and the CF directions). They are labelled together in figures 6 and 7 with the black dash arrow and corresponding modal group name beside. We can see that within the same modal group, the maximum CF and IL

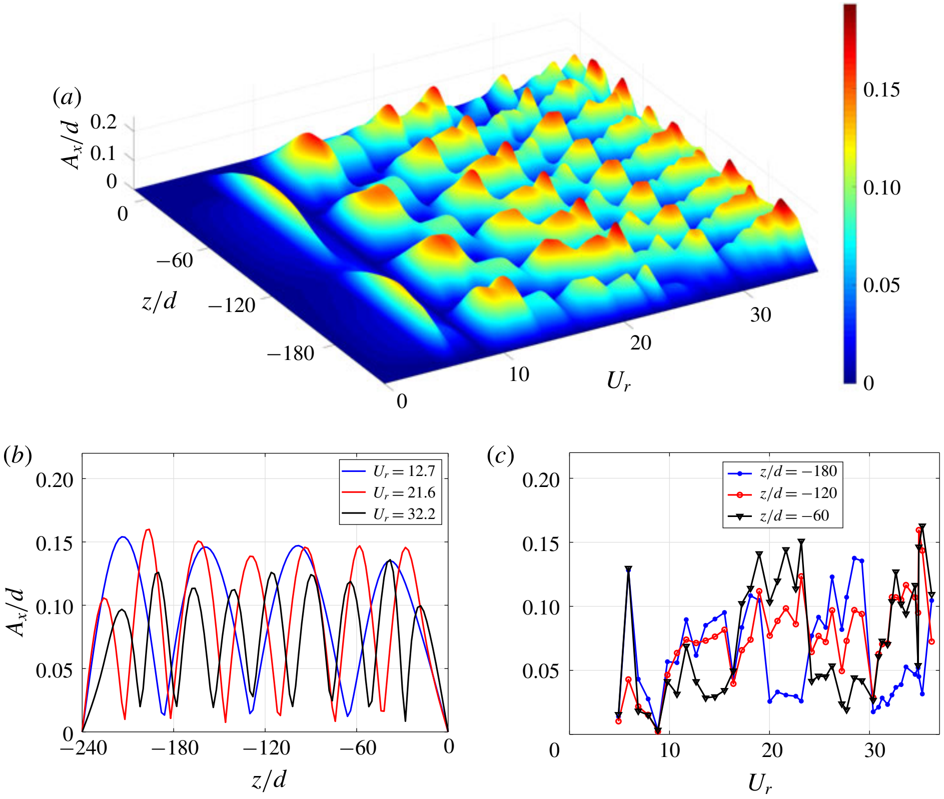

FIGURE 5. (Colour online) Experimental results of the displacement response in the IL direction: (*a*) 3-D visualization of the displacement response as a function of z/d and U_r; (*b*) displacement response along the flexible model at $U_r = 12.7$, 21.6 and 32.2; (*c*) displacement response versus U_r at locations of $z/d = -180$, -120 and -60. Note that the displacement response here is presented based on 1/10th highest peak measurement. In the current experiment, as U_r increases, the flexible model vibrates at a higher mode number up to 11th in the IL direction. A symmetric amplitude response along the model span is observed in our experiments.

amplitudes of the displacement response monotonically increase with U_r, but whenever there is a switch of the dominant mode in either the IL or the CF direction, the maximum amplitudes in both directions drop, except the switch from ‘5/3’ to ‘6/3’ in the CF direction. Similar phenomena of dropping of the displacement response between modes have been reported by Chaplin *et al.* (2005*b*) on a larger scale model in a non-uniform current. Moreover, it should also be noted that while the IL mode switch accompanies the CF mode switch, the former jumps twice more frequently in order to comply with the doubling of the CF mode number. Here, we conclude that in the current experiment there are two types of the modal group: group ‘$2n : n$’ and group ‘$2n - 1 : n$’, such as ‘4/2’ and ‘5/3’ shown in figure 6.

The response frequency ratios of the IL and the CF vibration are shown in figure 6 and figure 7, respectively. We see that in each modal group, the response frequency ratio in both the IL and the CF direction changes in a stepped rather than a linear relationship with U_r. In particular, in each modal group, the response frequency ratio stays on the average the same, but it changes to a different value whenever the

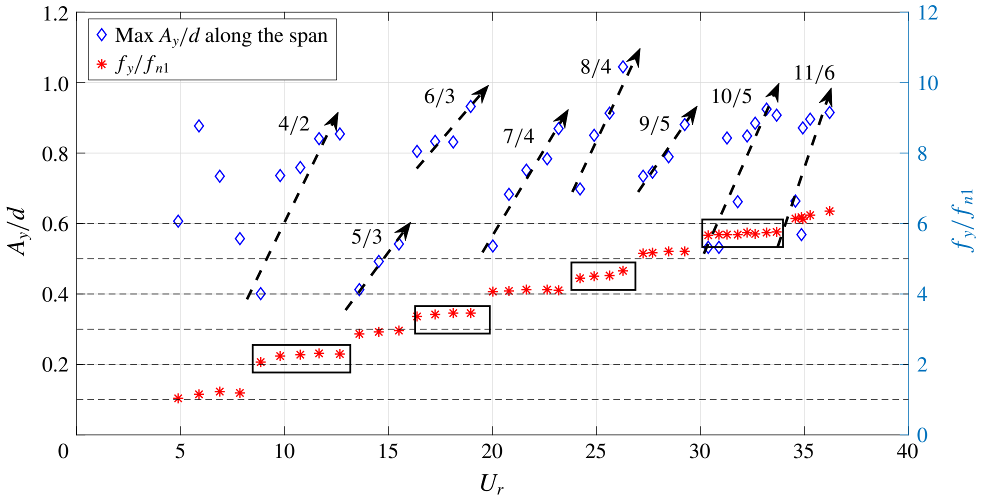

FIGURE 6. (Colour online) Frequency ratio and maximum amplitude of the CF displacement along the span versus U_r. Red stars, frequency ratio f_y/f_{n1}; blue diamonds, maximum amplitude of the CF displacement. Cases in the same modal group (same dominant mode in both the IL and the CF directions) are labelled together with the black dashed arrow. Starting from $U_r = 8.84$, in the same modal group the maximum of A_y/d monotonically increases with U_r, but during the modal group switch, both the maximum of A_y/d and the frequency ratio f_y/f_{n1} jump. The f_y/f_{n1} of the '$2n:n$' modal group highlighted by the black box, for example modal group '6/3', shows that the actual vibration frequency is larger than the natural modal frequency predicted in still water.

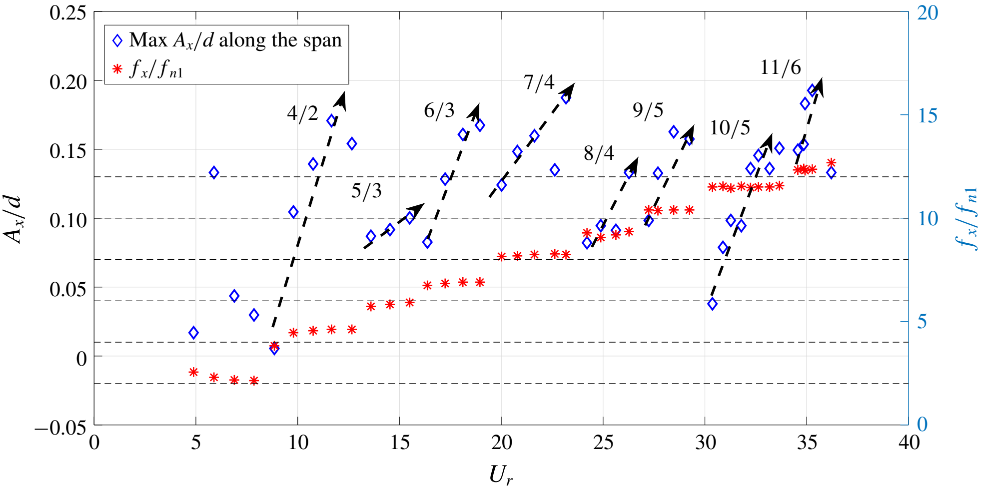

FIGURE 7. (Colour online) Frequency ratio and maximum amplitude of the IL displacement along the span against U_r. Red stars, frequency ratio f_x/f_{n1}; blue diamonds, maximum amplitude of the IL displacement. Starting from $U_r = 8.84$, in the same modal group the maximum of A_x/d monotonically increases with U_r, but during the modal group switch, both the maximum of A_x/d and the frequency ratio f_x/f_{n1} jump.

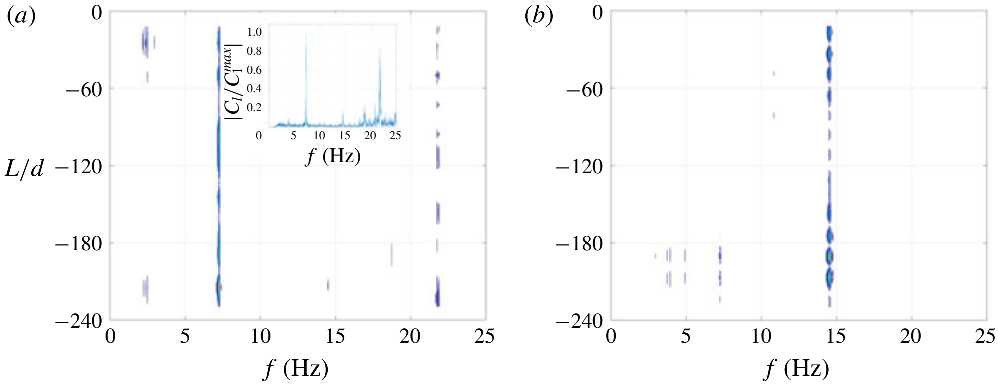

FIGURE 8. (Colour online) Frequency response of the reconstructed fluid forces along the span at $U = 0.19\ \mathrm{m\ s^{-1}}$ ($U_r = 18.1$): (*a*) in the CF direction, apart from the 1st harmonic (7.27 Hz), the 3rd force harmonic (21.81 Hz) is found, even though it is barely visible in the displacement frequency response in figure 3(*a*), and the inset figure plots the frequency response of the reconstructed fluid forces in the CF direction at $z/d = -160$; (*b*) in the IL direction, the 2nd harmonic (14.54 Hz) dominates.

dominant mode either in the IL or the CF direction switches. More interestingly, as highlighted by the black box in figure 6, the response frequency of the '$2n:n$' modal group is larger than the predicted nth modal natural frequency in still water, which indicates that the average added mass coefficient along the model in the CF direction is smaller than 1.0. On the contrary, the frequency response of the '$2n-1:n$' modal group stays close to the predicted natural frequency.

3.2. *Inverse hydrodynamic coefficients distribution along the flexible model and comparison with the two-dimensional rigid cylinder hydrodynamic database*

The fluid forces along the flexible model are reconstructed from the measured motion data using the method presented in appendix B. Shown in figure 8, the case of $Ur = 18.1$ ($U = 0.19\ \mathrm{m\ s^{-1}}$) is selected to represent the force frequency response along the model. In the CF direction, there are two clear force components corresponding to the 1st and 3rd harmonics, at 7.27 Hz and 21.81 Hz, despite the fact that the 3rd harmonic motion can be barely detected in the displacement response shown in figure 3(*a*). The existence of such a high harmonic force component in the CF direction has been reported in a previous experiment on the rigid cylinder vibration (Du, Jing & Sun 2014). In the IL direction, the 2nd harmonic force component at 14.54 Hz dominates the response.

The relative motion between the cylinder and the forming vortices can significantly alter the VIV response, as pointed out by Sarpkaya (2004). The forced vibration experiment on rigid cylinders with combined harmonic IL and CF motions by Dahl, Hover & Triantafyllou (2006) revealed that in addition to the imposed vibration frequency and amplitudes in the IL and the CF directions, the phase angle between the IL and the CF motions, θ, is also a critical parameter that determines the variation of the hydrodynamic coefficients. In particular, a counter-clockwise trajectory, defined as a figure-eight motion where the IL velocity at the CF motion extremes is against the oncoming stream, results in strong energy-in, from the flow to the structure.

Sinusoidal motions were prescribed in the IL and the CF directions, $y=\cos(\omega t)$ for the CF motion and $x=\cos(2\omega t+\theta)$ for the IL motion.

A key question is whether the hydrodynamic coefficients from the two-dimensional (2-D) forced vibration of the rigid cylinder can predict the fluid forces along the flexible cylinders in uniform flow. Based on equations (B 4) to (B 6) (in appendix B), the hydrodynamic coefficients along the flexible model were calculated and were compared directly with the newly constructed hydrodynamic coefficients database, that also includes the database of the forced IL and CF coupled vibration performed by Dahl (2008) and Zheng *et al.* (2014*a*). For hydrodynamic coefficient comparison, the following four parameters (V_r, A_x/d, A_y/d and θ) need to be matched between the flexible cylinder vibration at each location and the rigid cylinder prescribed motion.

In figures 9(*a*) and 9(*b*), we plot the A_x/d and A_y/d, as well as θ along the flexible model at $U_r=12.66$ of modal group '4/2' and at $U_r=13.61$ of modal group '5/3', respectively. The black dashed line in figures 9(*a*) and 9(*b*) marks a phase angle value of $\theta=\pi$ (a phase value in the range $\theta\in[0,\pi]$ represents a counter-clockwise trajectory, while $\theta\in[\pi,2\pi]$ represents a clockwise trajectory). From figures 9(*c*) to 9(*j*), we show the four hydrodynamic coefficients distribution along the model and compare them against the rigid cylinder hydrodynamic database: C_{lv}, C_{my}, C_{dv} and C_{mx}. Two important points can be noted. First, based on the phase and displacement response, we observed that at the IL node, the phase undergoes a π change, and this causes a discontinuous distribution of phase along the model, as also noted in (Bourguet, Karniadakis & Triantafyllou 2013). Second, by comparing the flexible model coefficients with those of the rigid cylinder experiments, despite the difference in Reynolds numbers, ($O(10^2)$ to $O(10^3)$ for the flexible cylinder experiment, and $O(10^4)$ for the rigid cylinder experiment), a good match is found for hydrodynamic coefficients between rigid and flexible cylinder experiments. It is worth noting that for the rigid cylinder CF-only free vibration in uniform flow, the experiment conducted by Govardhan & Williamson (2006) showed that A_y/d increases from 0.6 to 1.3 as *Re* increases in from 500 to 33 000, but the current research focuses on the rigid and flexible cylinders in both IL and CF directions, for which both the experimental measurements by (Dahl *et al.* 2010) and current results show that A_y/d is not strongly dependent on *Re* as the CF only vibrations are.

Furthermore, we note from figures 9(*c*) and 9(*d*) for the lift coefficient in-phase with the velocity C_{lv}, that the region of positive energy transfer from the fluid to the structure is mainly associated with a counter-clockwise (CCW) trajectory. This was first established in the rigid cylinder experiment by Dahl *et al.* (2006) and flexible cylinder simulations by Bourguet *et al.* (2011).

The added mass coefficient plays an important role in VIV because it can vary as a function of frequency and amplitude, and can alter the natural frequency of the system significantly. For example, in figures 9(*e*) and 9(*f*), the added mass coefficient in the CF direction C_{my} is found to be drastically different between $U_r=12.66$ and $U_r=13.61$. Here C_{my} is found larger than 0 along the flexible model at $U_r=13.61$ of the modal group '5/3'; on the contrary, at $U_r=12.66$ of the modal group '4/2', both negative and positive values of C_{my} can be observed at different locations of the model. At $U_r=12.66$, it can be seen that the positive and negative regions of C_{my} are separated by a jump at the IL node, where θ changes abruptly by π. In contrast to the large variation C_{my} along the model, the added mass coefficient in the IL direction, C_{mx}, remains flat.

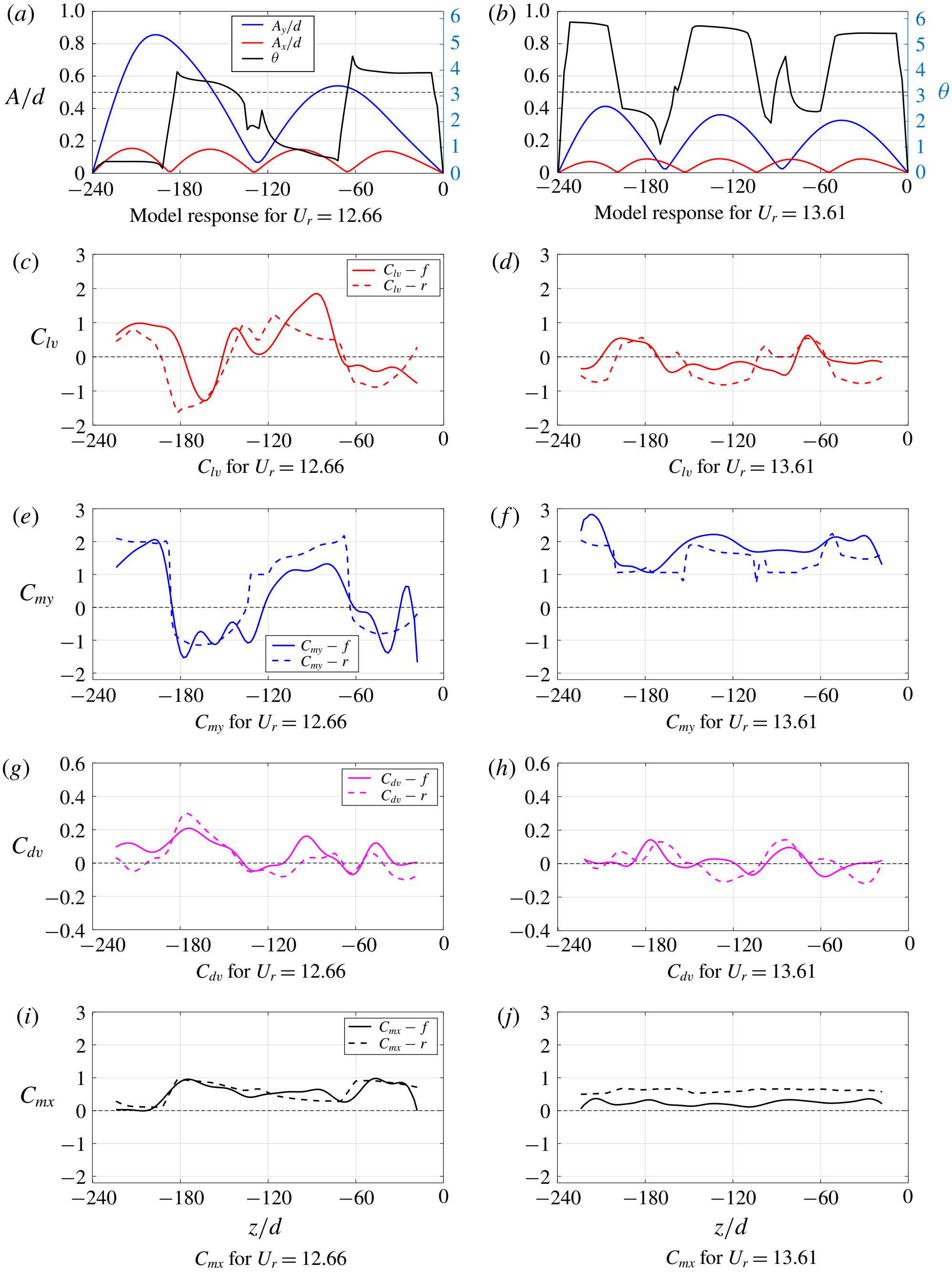

FIGURE 9. (Colour online) Displacement response and reconstructed hydrodynamic coefficients. (*a*,*c*,*e*,*g*,*i*), $U_r = 12.66$ of modal group '4/2'; (*b*,*d*,*f*,*h*,*j*), $U_r = 13.61$ of modal group '5/3'. Good agreement can be observed between the hydrodynamic coefficient distribution along the span of the flexible model (solid line) and the predicted value from the rigid cylinder database (dashed line). The two different modal groups, '4/2' and '5/3', exhibit drastically different qualitative behaviour in the added mass coefficient distribution along the model.

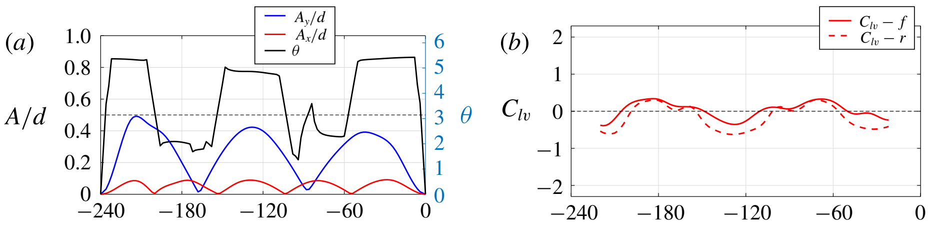

Model response at $U_r = 14.54$

C_{lv} distribution at $U_r = 14.54$

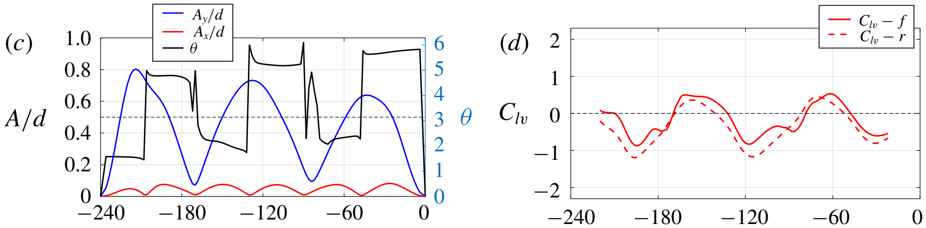

Model response at $U_r = 16.38$

C_{lv} distribution at $U_r = 16.38$

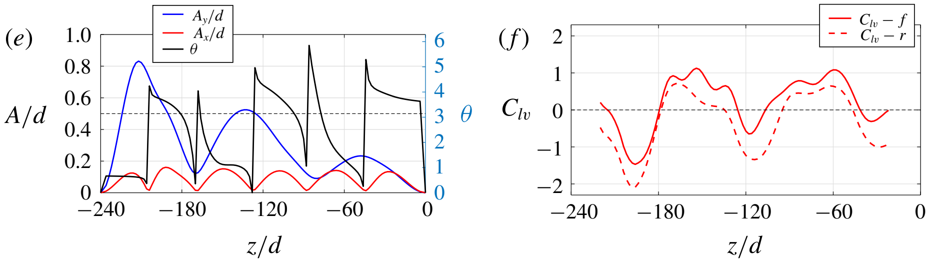

Model response at $U_r = 18.1$

C_{lv} distribution at $U_r = 18.1$

FIGURE 10. (Colour online) Experimental results of the displacement and the phase response (*a*,*c*,*e*) and C_{lv} distribution (*b*,*d*,*f*) along the model: (*a*,*b*) $U_r = 14.54$; (*c*,*d*) $U_r = 16.38$; (*e*,*f*) $U_r = 18.1$. As the reduced velocity U_r increases, the asymmetry of the CF amplitude (solid blue line) increases.

3.3. *Cross-flow asymmetric response and distribution of lift coefficient in-phase with the velocity*

Figure 10 presents the amplitude, phase response, and C_{lv} distribution along the flexible model at $U_r = 14.54$ of the modal group ‘5/3’, $U_r = 16.38$ of the modal group ‘6/3’ and $U_r = 18.1$ of the modal group ‘6/3’. For all three values of U_r, the cylinder responds in the 3rd mode in the CF direction. With increasing U_r, the distribution of the CF displacement changes from a small and symmetric response to an asymmetric response with a prominent peak. In figure 11, we plot the relative phase α of the oscillation at different locations along the flexible model span in the CF direction. The relative phase α is defined as zero at $z/d = -240$ and as the angle of the oscillation at each location. Comparing the blue line of $U_r = 14.54$ and the black line of $U_r = 18.1$ in figure 11, as the CF response changes from symmetric to asymmetric, the α distribution has a smoother transition at the CF node, which indicates a stronger mixture of travelling and standing wave responses (Bourguet *et al.* 2013).

Comparing the amplitude response with the C_{lv} distribution, four interesting points can be raised. First, in general the rigid cylinder database can capture the distribution of C_{lv} along the model. Second, the θ values corresponding to the CCW trajectory

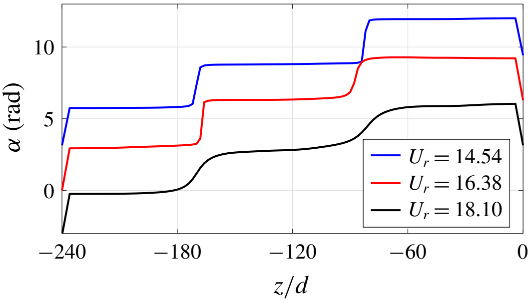

FIGURE 11. (Colour online) Relative phase α of the CF vibration at different locations along the span of the flexible model for blue, $U_r = 14.54$; red, $U_r = 16.38$; black, $U_r = 18.1$. For visual clarity, we assign an offset for blue and black curves.

are associated with the positive energy-in from the fluid to the structure. Third, when the CF amplitude is smaller, the C_{lv} distribution also obtains a smaller amplitude both positively and negatively, shown in the comparison between $U_r = 14.54$ and $U_r = 16.38$ (see figure 10). Last, for the asymmetric CF response with a mixture of standing and travelling wave patterns, C_{lv} is also found asymmetrically distributed along the flexible model, with the region of large negative values associated with the large CF amplitude, shown in figure 10(f) at $U_r = 18.1$.

From the samples of C_{lv} measured via the rigid cylinder forced vibration in appendix D, we find that θ corresponding to the CCW motion are associated with the positive C_{lv} when A_y/d is small, while C_{lv} is largely negative for clockwise motion. In addition, C_{lv} decreases with increasing A_y/d and A_x/d. In the experiment, when the flexible cylinder vibrates at the onset of the 3rd mode in the CF direction at $U_r = 14.54$, the amplitude response is small, as the true reduced frequency of the vibration is large and far away from the Strouhal frequency. It is similar to the low mass ratio rigid cylinder free vibration at the start of the initial branch with a large reduced frequency corresponding to small CF amplitudes (Jauvtis & Williamson 2003). With the increase of U_r, the true reduced frequency of the flexible cylinder decreases and gets close to the Strouhal frequency, so the fluid and structure coupling effect becomes stronger. This results in a larger CF amplitude associated with a stronger energy exchange between the fluid and the structure in the CF direction. Therefore, comparing $U_r = 16.38$ to $U_r = 14.54$, shown in figures 10(b) and 10(d), we see a larger magnitude for both negative and positive C_{lv} distribution along the model span. Further increasing U_r, the CF amplitude tends to get larger, and if the CF amplitude remains symmetric and hence increases altogether along the span, more energy is required from the fluid to the structure, as the structure dissipates more energy via damping over one vibration cycle. However, in general, C_{lv} decreases with increasing A_y/d (such a trend can be seen in figure 27 in appendix B of the rigid cylinder forced vibration) and therefore the energy balance between the fluid and the structure cannot be maintained. Subsequently, due to the alternative clockwise (CW) and CCW θ distribution along the flexible model, the asymmetric response in the CF direction is allowed to grow. A large amount of fluid energy transfers into the flexible model in its small A_y/d and CCW θ region, and then transmits inside the flexible model, which leads to the appearance of a stable travelling wave. Due to the finite length of the model, a standing wave response with a large amplitude forms close to the boundary due to the reflection, and the ambient fluid helps the structure to dissipate energy at that region with a large CF amplitude.

3.4. *Modal group switch and added mass variation in and between modal groups*

In the previous sections we showed that the sectional hydrodynamic coefficients for a flexible cylinder are predicted accurately by the forced vibration experiment on rigid cylinders. In this section, we focus on understanding why the added mass coefficient in the CF direction undergoes such large variations and why it is different for different modal groups.

The spatial mean added mass coefficient $\overline{C_m}$ in either the IL or the CF direction for the flexible cylinder is calculated for all U_r based on the following equation:

$$\overline{C_m} = \frac{1}{L}\int_0^L C_m(z)\,\mathrm{d}z. \tag{3.1}$$

The reconstructed $\overline{C_m}$ from the motion data and the corresponding predicted values from the rigid cylinder experiments are plotted together against U_r in figure 12 for $\overline{C_{my}}$ and figure 13 for $\overline{C_{mx}}$. Both figures show good agreement between the flexible cylinder measurements and the rigid cylinder prediction. We obtained that the averaged relative difference of $\overline{C_{my}}$ between the measurement of the flexible cylinder ($250 \leqslant Re \leqslant 2\,300$) and the prediction of the rigid cylinder forced vibration ($Re = 5\,715$), namely $(|\overline{C_{my}^{rigid}} - \overline{C_{my}^{flex}}|)/|\overline{C_{my}^{flex}}|$, is around 17.4 %. The $\overline{C_{my}}$ exhibits different behaviour in the modal group '$2n:n$' (highlighted in figures 12 and 13 with a shaded region) and the modal group '$2n-1:n$'. Values of $\overline{C_{my}}$ in the modal group '$2n:n$' are close to 0.5, which drives the natural frequency of the flexible model to larger values than the predicted nth modal frequency in still water, assuming $C_m = 1.0$. In contrast, $\overline{C_{my}}$ in the modal group '$2n-1:n$' is larger than 1.0 (the black dashed line denotes $\overline{C_{my}} = 1.0$ in figure 12). The predicted true modal frequencies f_{nx}^{true} and f_{ny}^{true} for the IL and the CF vibrations are given by equation (3.2) as follows:

$$\left.\begin{aligned} f_{ny}^{true} &\simeq \overline{f_{ny}^{true}} = \frac{n}{2L}\sqrt{\frac{\overline{T}}{(\mu + \overline{\mu_y})}},\\ f_{nx}^{true} &\simeq \overline{f_{nx}^{true}} = \frac{m}{2L}\sqrt{\frac{\overline{T}}{(\mu + \overline{\mu_x})}}, \end{aligned}\right\} \tag{3.2}$$

where $\overline{\mu_y} = \overline{C_{my}}\rho(\pi/4)D^2$ is the spatial mean added mass per unit length in the CF direction, $\overline{\mu_x} = \overline{C_{mx}}\rho(\pi/4)D^2$ is the spatial mean added mass per unit length in the IL direction and $\overline{T}$ is the average tension along the model. The difference between f_n^{true} and $\overline{f_n^{true}}$ is addressed in appendix C. In the current experiment, $\overline{C_{my}}$ shows a large variation between different modal groups, while $\overline{C_{mx}}$ does not vary much and stays close to 0.5, as shown in figure 13.

As pointed out in Dahl *et al.* (2010), the effective IL and CF added mass coefficients vary collaboratively in order to reach a true natural frequency ratio of $f_{nx}^{true}/f_{ny}^{true} = 2.0$, and a dual resonance of stable oscillations in both the IL and the CF directions can be achieved. For the uniform flexible cylinder VIV, the same criterion should be held for the fluid added mass, as the system's true natural frequency has to be altered in order to match the external frequency. It is shown in equation (3.3) that the system's true natural frequency, the system vibration frequency and the external disturbance frequency, namely the shedding vortex frequency should coincide with each other, i.e.

$$\left.\begin{aligned} f_y = f_{ny}^{true}, \quad f_x = f_{nx}^{true},\\ f_x = 2f_y = 2f_v, \end{aligned}\right\} \tag{3.3}$$

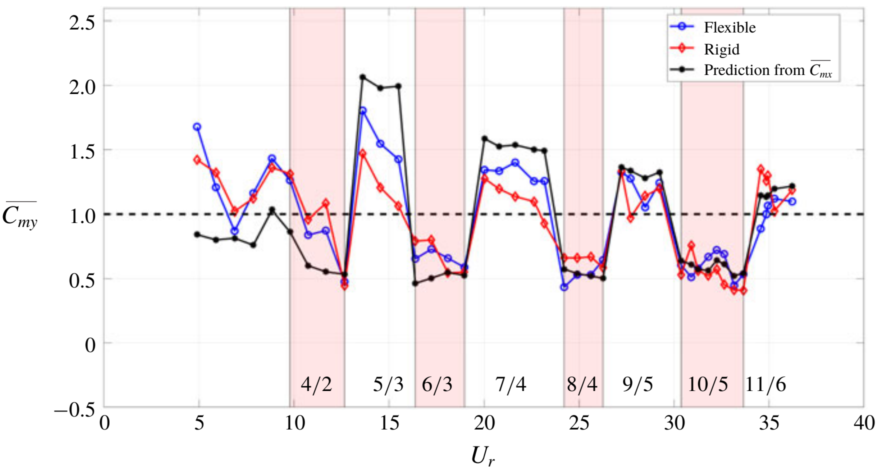

FIGURE 12. (Colour online) Spatial mean added mass coefficient in the CF direction $\overline{C_{my}}$ as a function of U_r. Here $\overline{C_{my}} > 1.0$ corresponds to the modal group '$2n-1:n$' and $\overline{C_{my}} < 1.0$ corresponds to the modal group '$2n:n$'. The shaded area highlights the modal group '$2n:n$'.

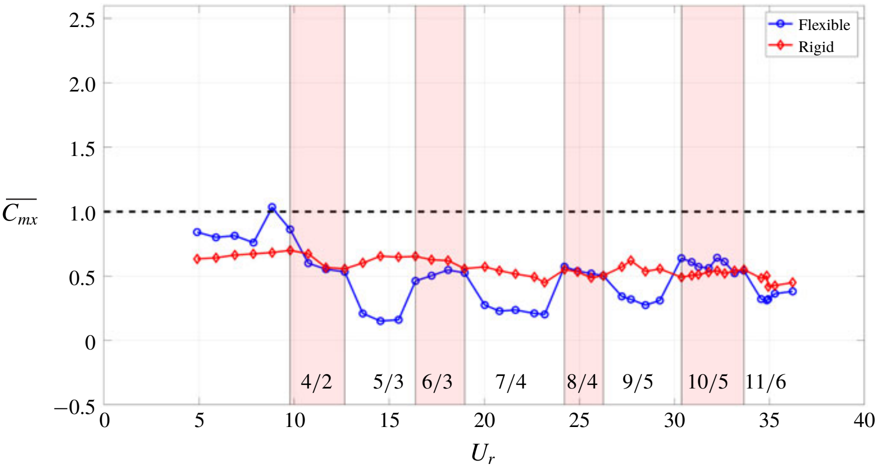

FIGURE 13. (Colour online) Spatial mean added mass coefficient in the IL direction $\overline{C_{mx}}$ as a function of U_r. Unlike $\overline{C_{my}}$, $\overline{C_{mx}} < 1.0$ for all modal groups. The shaded area highlights the modal group '$2n:n$'.

where f_x and f_y are the vibration frequencies of the flexible cylinder in the IL and the CF directions, respectively, f_{nx}^{true} and f_{ny}^{true} are the true natural frequencies of the flexible cylinder in the IL and the CF directions and f_v is the vortex shedding frequency in the cylinder wake. When $m=2n$, the added mass coefficient in the IL and the CF directions is given by the following equation, based on equations (3.2) and (3.3),

$$\overline{C_{my}} \simeq \overline{C_{mx}}. \tag{3.4}$$

When $m = 2n - 1$, we also derived the following equation for the added mass coefficient in the IL and the CF directions,

$$\overline{C_{my}} \simeq \frac{4n^2 - (2n-1)^2}{(2n-1)^2} m^* + \frac{4n^2}{(2n-1)^2} \overline{C_{mx}}. \tag{3.5}$$

In figure 12, we plot the predicted $\overline{C_{my}}$ (black line) based on the $\overline{C_{mx}}$ in figure 13 (blue line). Equations (3.4) and (3.5) give a large variation of the $\overline{C_{my}}$ between different modal groups from a relatively constant $\overline{C_{mx}}$ over U_r.

Next we focus on $U_r = 10.75$ of the modal group '4/2', $U_r = 12.66$ of the modal group '4/2' and $U_r = 13.61$ of the modal group '5/3' in order to explain how the added mass changes when U_r increases in and between modal groups.

Figures 14 and 15 present the C_{my} and C_{mx} predictions as a function of V_r and θ from the forced oscillating rigid cylinder with matched A_x/d and A_y/d at different locations along the flexible cylinder at $U_r = 10.75$, $U_r = 12.66$ and $U_r = 13.61$. A detailed description of the added mass coefficient in both the IL and CF directions with respect to V_r and θ is presented in appendix D. The grey transparent slices highlight the true reduced velocity V_r and the solid black line denotes the θ distribution. The intersection between the C_{my} and C_{mx} contour and the θ line is highlighted with the yellow diamond, denoting the predicted sectional C_{my} and C_{mx} of the flexible model via the rigid cylinder hydrodynamic database with the same values of A_y/d, A_x/d, V_r and θ.

The flexible cylinder in uniform flow vibrates at the same frequency along the entire model, resulting in the same V_r at each location. The θ distribution has a π phase jump at the IL node. As shown from the rigid cylinder forced vibration experiment (appendix B), θ has a strong influence on C_{my}, and therefore C_{my} changes drastically at the IL node along the flexible cylinder. Furthermore, the effect of A_x/d and A_y/d on C_{my} is weak, so inside a half-wavelength of the IL response mode, C_{my} keeps a relatively constant value, which results in a stepped distribution of C_{my}, as shown in figure 14. In addition, similar to C_{my}, C_{mx} also distributes along the model in a stepped fashion, but compared to the large variation of C_{my} distribution, C_{mx} changes slightly, as shown in figure 15.

Here we give more details on what happens to the fluid added mass distribution with an increasing U_r, and explain why the flexible cylinder switches modal group. To begin with, as U_r increases from 10.75 to 13.61 (correspondingly, the towing velocity changes from 0.11 m s^{-1} to 0.14 m s^{-1}), the vortex shedding frequency tends to increase. In order to maintain a stable flexible cylinder VIV in the lock-in region, for the CF vibrations, the three frequencies have to be the same: f_y, f_v and f_{ny}^{true}, shown in equations (3.2) and equations (3.3). In each experiment, the mean tension T, length L and structural mass per unit length μ of the model are fixed, and only the mode number n and the spatial average fluid added mass per unit length $\overline{\mu}$ can be altered to change the structural natural frequency.

Figures 14(a) and 14(b) shows that with the increase of U_r from 10.75 to 12.66, the flexible model still remains in the same modal group, but in order to match f_{ny}^{true} and the increasing f_v, the V_r and θ distribution are adjusted to find a proper combination of the fluid added mass distribution. Comparing figure 14(b) at $U_r = 12.66$ to figure 14(a) at $U_r = 10.75$, the sectional C_{my} at some locations along the model approaches its negative minimum, predicted by the rigid cylinder forced vibration experiment. Further increasing U_r (the towing velocity increases in the experiment), if the flexible model is in the same modal group, a smaller $\overline{\mu_y}$ is required in order to increase f_{ny}^{true} for

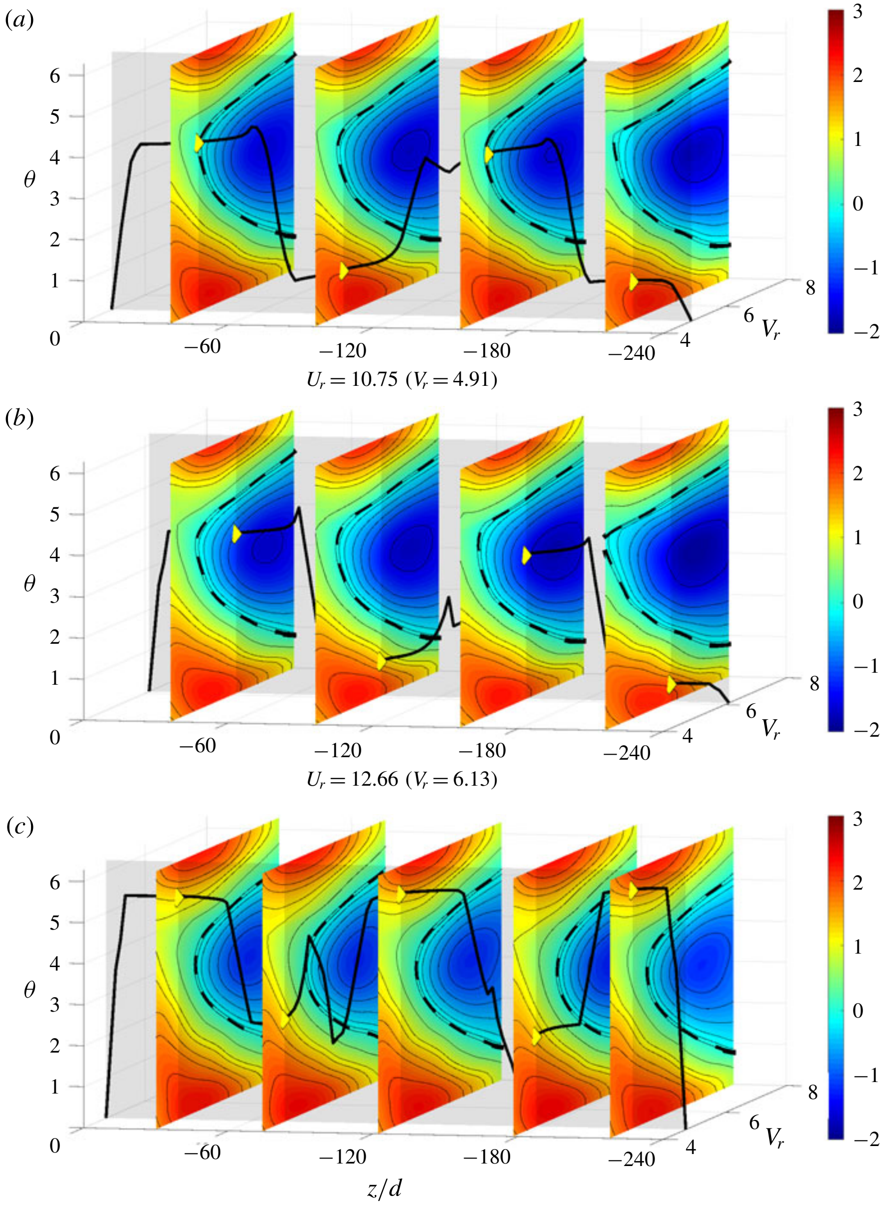

$U_r = 10.75$ ($V_r = 4.91$)

$U_r = 12.66$ ($V_r = 6.13$)

$U_r = 13.61$ ($V_r = 4.73$)

FIGURE 14. (Colour online) The C_{my} values along the span of the flexible model interpolated from the rigid cylinder forced vibration experiments. The colour contours of C_{my} are computed as a function of V_r and θ from the forced oscillating rigid cylinder with the matched A_x/d and A_y/d. The θ distribution (the solid black line) and V_r (the shaded plane) highlight the C_{my} value at each contour plane (the yellow diamond).

higher f_v. However, no corresponding V_r and θ distribution can be found, as at smaller U_r, C_{my} at different locations along the flexible model has already reached or is close to the negative minimum. Note here that not only the fluid added mass has to be

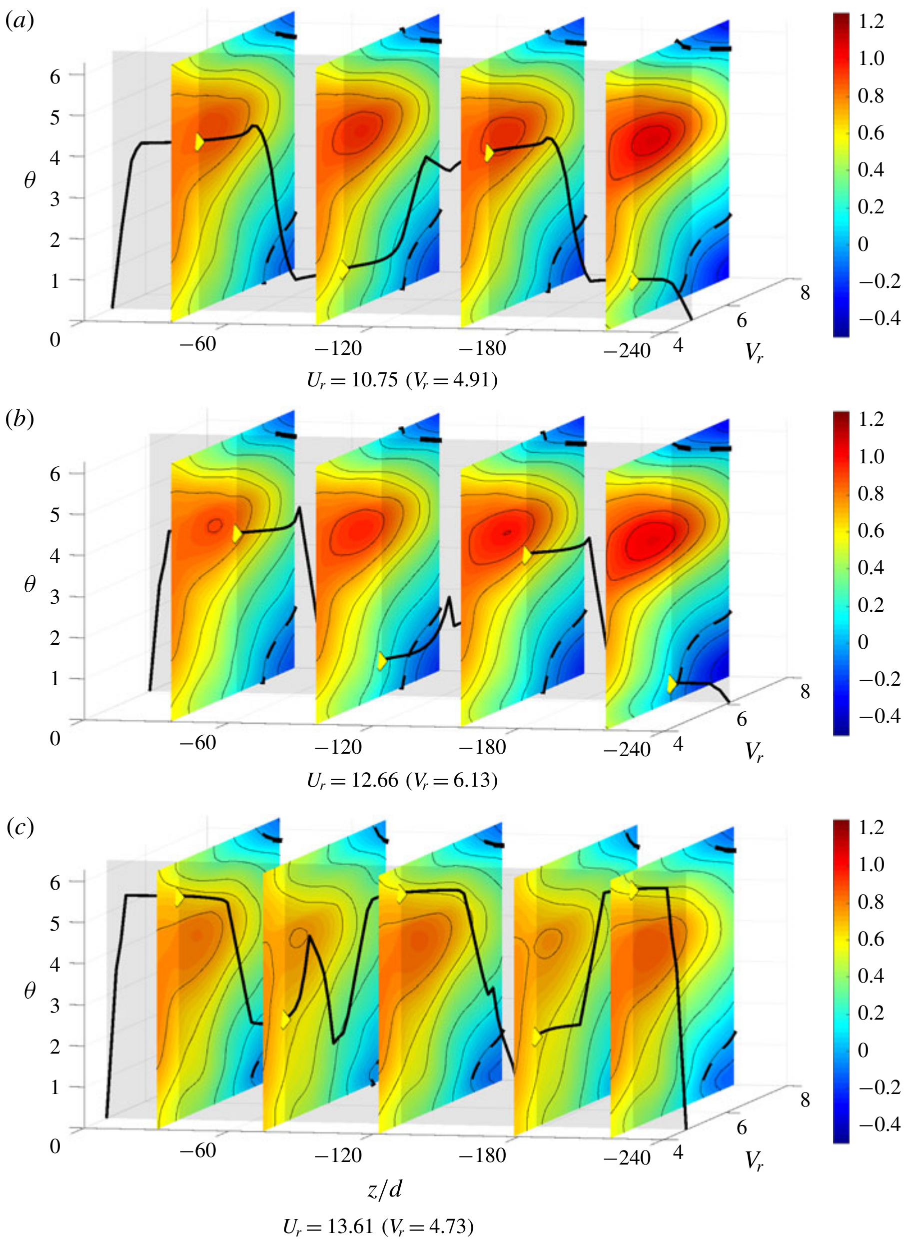

(a) $U_r = 10.75$ ($V_r = 4.91$)

(b) $U_r = 12.66$ ($V_r = 6.13$)

(c) $U_r = 13.61$ ($V_r = 4.73$)

FIGURE 15. (Colour online) The C_{mx} values along the span of the flexible model interpolated from the rigid cylinder forced vibration experiments. The colour contours of C_{mx} are computed as a function of V_r and θ from the forced oscillating rigid cylinder with the matched A_x/d and A_y/d. The θ distribution (the solid black line) and V_r (the shaded plane) highlight the C_{my} value at each contour plane (the yellow diamond).

adjusted to agree with equations (3.2) and (3.3), but also the net energy between the structure and the fluid should be balanced, and hence there are also constraints on C_{lv} and C_{dv}.

With no possibility of finding a proper added mass distribution to keep the same modal response in the CF direction, the mode number of the flexible model vibration needs to switch. Comparing figure 14(*c*) at $U_r = 13.61$ to figure 14(*b*) at $U_r = 12.66$, the flexible model switches from the modal group '4/2' to the modal group '5/3'. With such mode number switch, the structure natural frequency experiences a big jump – for example, it jumps from $2f_{n1}$ for $U_r = 12.66$ to $3f_{n1}$ for $U_r = 13.61$ in the CF direction. However, the vortex shedding frequency increases slightly due to a small increase of U_r, so the θ distribution and the V_r value of the flexible model have to adjust accordingly, as shown in figure 14.

4. Coupled fluid-structure analysis: wake visualization via LES

For VIV problems, a vortical flow pattern analysis is crucial for a better understanding of the mechanisms of coupled interaction between the fluid and the structure. In this section, we provide results of wake visualization obtained through numerical simulation of the flexible model, using uniform tension and the same model structural properties as in the experiment. A total of eight cases, from $U_r = 10.75$ to $U_r = 17.22$ are chosen for the simulation, covering a modal group switch from '4/2' to '6/3'. Since the main focus of this section is to discuss the local and overall 3-D vortical patterns around and in the wake of the flexible cylinder and their effects on the model response and the fluid forces, the validation of the numerical model is presented in appendix E, including an extensive comparison with the flexible cylinder experimental results.

Figures 16 and 17 present the simulated results of the amplitude response, 3-D wake patterns and the hydrodynamic coefficients distribution along the flexible cylinder at $U_r = 14.54$ of the modal group '5/3' and $U_r = 17.22$ of the modal group '6/3'. The vortices are represented by isosurfaces of $Q = 0.1$ and coloured by ω_z. We observe that the vortex formation behind the model can be separated into different cells along the flexible span. For example, figure 17 at $U_r = 17.22$ of the modal group of '6/3' shows that the flexible cylinder vortical wake can be divided into six zones consisting of two patterns, alternatively distributed along the spanwise direction. These two patterns correspond to one region of clear straight vortex tubes and the other one of wavy vortex tubes with strong streamwise vortices, and such a pattern of the three-dimensional instability has been reported for the rigid cylinder vibration both experimentally (Wu *et al.* 1996) and numerically (Thompson, Hourigan & Sheridan 1996); the vortical tubes of the two regions connect with each other in ways that are reminiscent of the patterns noted in Techet, Hover & Triantafyllou (1998).

In addition, by comparing the vortex patterns and C_{my} distribution along the span of the flexible cylinder, we found that the vortex shedding mode and the sign of the sectional C_{my} are strongly correlated: the mode 'P+S' or '2P' appears in the region of negative C_{my}; the mode '2S' is related to the positive C_{my} region. In figures 16 and 17, the blue shaded region denotes the locations along the flexible model where the vortex mode 'P+S' or '2P' can be observed. This reveals a relationship between the sign of the sectional C_{my} and the local vortex shedding mode that the negative C_{my} is accompanied with the 'P+S' or '2P' vortex mode.

Carberry, Sheridan & Rockwell (2005) performed an experiment on controlled transverse-only oscillations of the rigid cylinder in uniform flow, and obtained that the phase between the oscillating lift force and cylinder motion jumped discontinuously when the vibration frequency was close to a threshold frequency (a frequency close to the Strouhal frequency of a fixed rigid cylinder in the flow). Such phase jump led

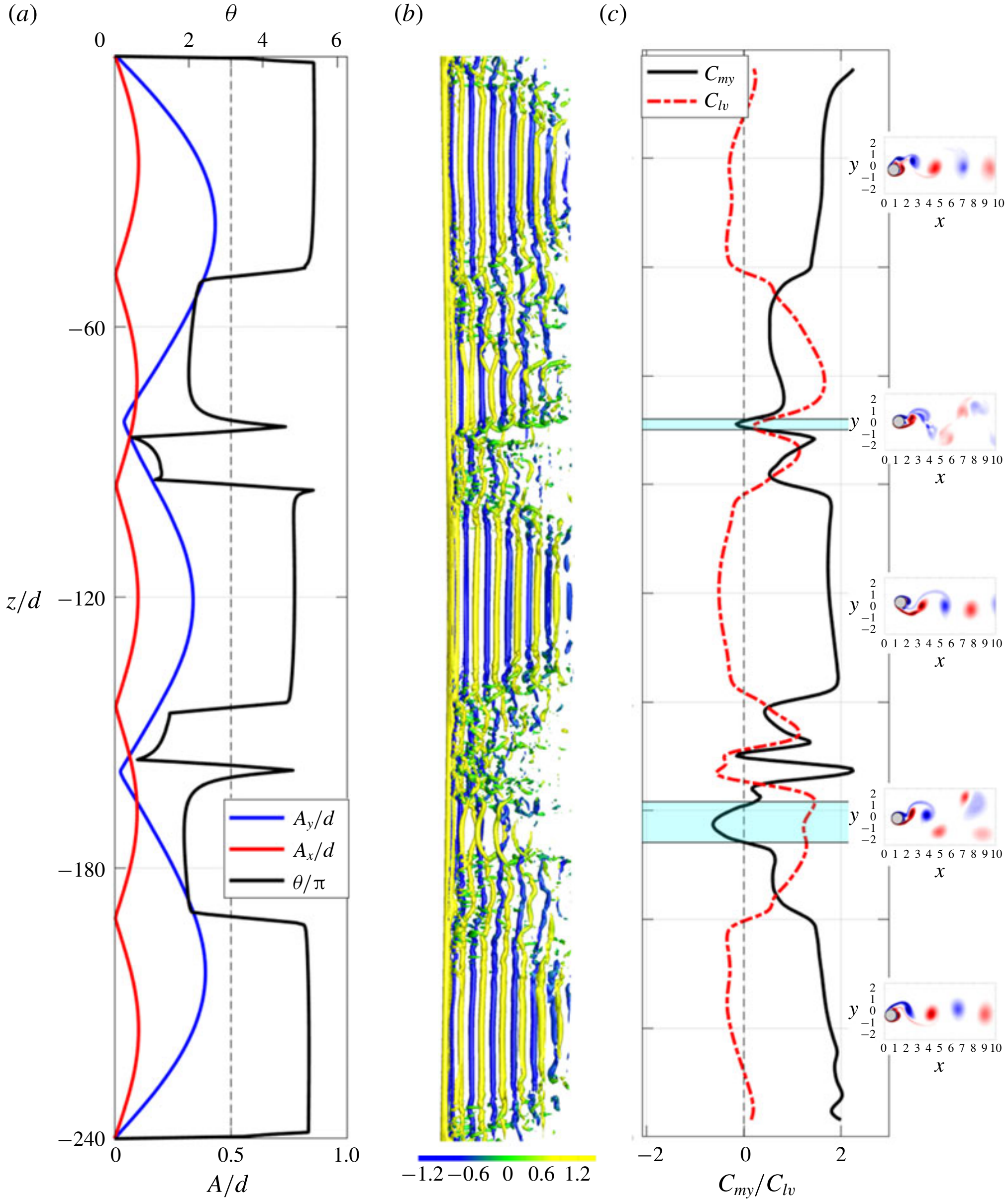

FIGURE 16. (Colour online) Simulation results at $Ur = 14.54$ of modal group '5/3' ($Re = 750$). (*a*) Amplitude and phase response along the span of the flexible cylinder, and the black dashed line denotes $\theta = \pi$; (*b*) snapshot of the vortices behind the flexible model. Here vortices are represented by isosurfaces of $Q = 0.1$ and coloured by ω_z; (*c*) hydrodynamic coefficients of C_{lv} (red dashed line) and C_{my} (black solid line) distribution along the span of the flexible cylinder, and the blue shaded region denotes the sections along the flexible cylinder where the 'P+S' or '2P' vortex mode is found locally, while in the white region, the '2S' vortex mode can be observed.

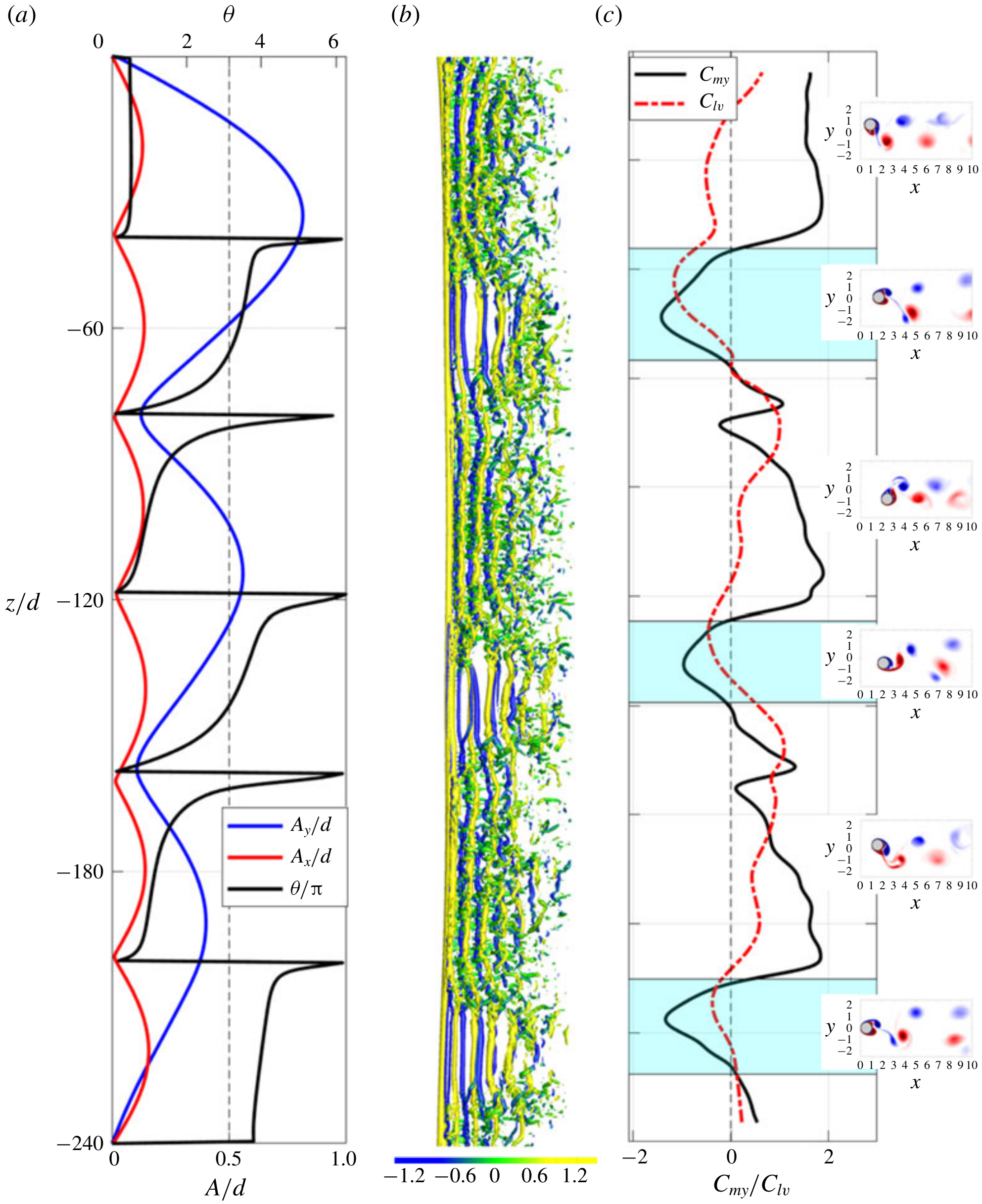

FIGURE 17. (Colour online) Simulation results at $Ur = 17.22$ of modal group '6/3' ($Re = 900$). (*a*) Amplitude and phase response along the span of the flexible cylinder, and the black dashed line denotes $\theta = \pi$; (*b*) snapshot of the vortices behind the flexible model. Here vortices are represented by isosurfaces of $Q = 0.1$ and coloured by ω_z; (*c*) hydrodynamic coefficients of C_{lv} (red dashed line) and C_{my} (black solid line) distribution along the span of the flexible cylinder, and the blue shaded region denotes the sections along the flexible cylinder where the 'P+S' or '2P' vortex mode is found locally, while in the white region, the '2S' vortex mode can be observed.

to a sign switch of C_{my} and a transition between the wake states: the mode '2P' with $C_{my} < 0$; the mode '2S' with $C_{my} > 0$.

Note that for the uniform flexible cylinder in uniform flow, the true reduced velocity V_r is constant along the entire model, so the appearance of the different vortex modes must be the result of the change in the phase θ of the IL and the CF trajectories, instead of the change in the frequency ratio between the vibration frequency and the Strouhal frequency.

4.1. *Three-dimensional wake structure behind the flexible cylinder: distortion of shed vortices at IL nodes*

In order to assess the spanwise correlation of the wake structure behind the flexible model, a frequency and phase analysis is applied to the cross-flow component of the flow velocity, located at three diameters downstream from the mean IL displacement.

Figures 18 and 19, each presents the PSD (subfigure *c*) and the phase distribution (subfigure *d*) of the cross-flow component of the flow velocity at $U_r = 14.54$ and $U_r = 17.22$, together with the IL and the CF amplitude response (subfigure *a*) and the PSD of the CF displacement (subfigure *b*). Comparing subfigures (*b*) and (*c*) from figures 18 and 19, it is shown that the 'lock-in' happens along the entire model span, as the CF vibration frequency is equal to the vortex shedding frequency everywhere. However, the phase analysis on the cross-flow velocity component reveals that at IL nodes the phase of the flow velocity changes drastically, whereas it keeps a relatively constant value along the half-wavelength between two adjacent IL nodes. At IL nodes, the phase θ between the IL and CF trajectory undergoes a phase jump by π, which leads to a change in the vortical structures, as reflected in the snapshots of the local vortex shedding around IL nodes over one vibration cycle in figure 18(*e*) at $U_r = 14.54$ and in figure 19(*e*) at $U_r = 17.22$. We can see that there is a shift of the vortex tubes (positive vortex in yellow) in space as well as a vortex pattern switch above and below the black dash line denoting one of the IL nodes along the flexible model.

Specifically, at $U_r = 17.22$, along the span of the cylinder, the vortices shed in cells that are separated by the IL nodes, and the relative motion between the local cylinder oscillation and vortex formation also breaks into the same cells, which explains the variation of the added mass along the flexible model span, shown in figure 17(*c*). At $U_r = 14.54$, the response is a modal group '5/3' (model group type '$2n - 1/n$'), but unlike case of $U_r = 17.22$, here the IL and CF nodes do not coincide with each other. As shown in figure 18, apart from the dislocation of the vortex tube around $z/d = -50$, $z/d = -94$, $z/d = -146$ and $z/d = -189$ where IL nodes reside in, an interesting phenomenon called the 'void' vortex shedding region could be observed at $z/L = -82$ and $z/L = -158$, both of which are CF nodes. A similar phenomenon has been reported experimentally by Gilbert & Sigurdson (2010) and Bangash & Huera-Huarte (2015). However, note that in the previous experiments, the 'void' regions appear at IL node and CF anti-node, which is different from the current simulation results. The difference may be due to different *Re*, vibration mode number and, perhaps more importantly, the IL vibration amplitude. Unlike the current simulation, the IL amplitude is much smaller than the CF amplitude in the aforementioned two experiments. The 'void' vortex shedding region is accompanied with the local vortex pattern change, e.g. an attached symmetric non-shedding vortex pair behind the cylinder as reported by Bangash & Huera-Huarte (2015), which leads to a large local variation of C_{my}, shown in figure 18 of $z/d = -70$ to $z/d = -90$ and $z/d = -150$ to $z/d = -170$.

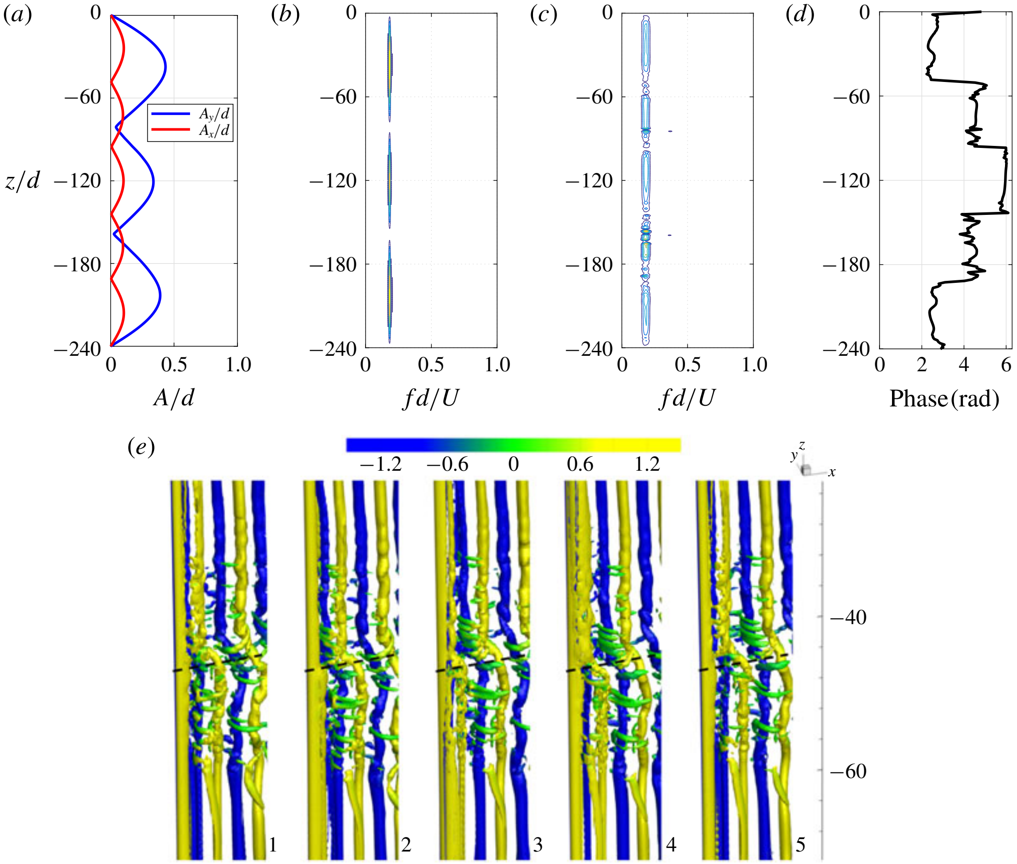

FIGURE 18. (Colour online) Linking the structural response (*a*–*d*) with the wake patterns (*e*). The simulation results show the dislocation of the shed vortex tubes around IL nodes at $U_r = 14.54$, highlighting the '2S' mode both above and below the black dashed line: (*a*) the IL and the CF amplitude response; (*b*) the PSD of the CF displacement; (*c*) the PSD of the CF flow velocity; (*d*) phase difference α of the CF flow velocity; (*e*) a series of snapshots of the vortex shedding over one period at $t=0$, $t=\frac{1}{4}T$, $t=\frac{1}{2}T$, $t=\frac{3}{4}T$ and $t=T$ from left to right, where T is the vibration period at $U_r = 14.54$. The black dashed line marks location $z/d = -48$. Note that the CF flow velocity is taken at three diameters downstream from the mean IL displacement and the vortices are represented by isosurfaces of $Q = 0.1$ and coloured by ω_z.

4.2. *Cross-sectional 2-D wake pattern: CF motion versus local vortex shedding*

As pointed out by Sarpkaya (2004), in flexibly mounted rigid cylinder experiments, a slight change of the relative motion between the cylinder oscillation and vortex formation can alter the hydrodynamic coefficients and the VIV response significantly. In this section, we use the 2-D snapshots of the spanwise field around the oscillating cylinder to explain the noted changes in the hydrodynamic coefficients.

Figures 20 to 23 provide five consecutive 2-D snapshots of the ω_z field around the flexible cylinder at a given location for $U_r = 14.54$ and $U_r = 17.22$ over one period of the CF vibration. In subfigures (*f*), we plot the time trace of the cylinder CF motion (black) as well as the lift coefficient (blue) at the corresponding location, with the red

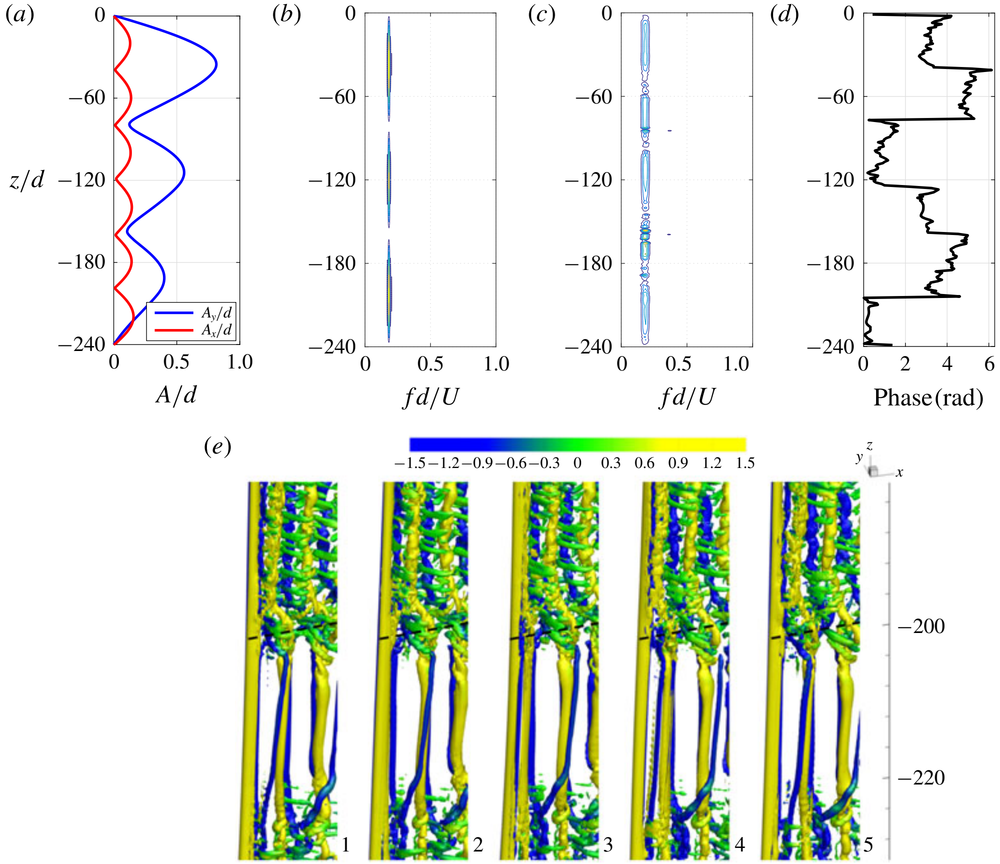

FIGURE 19. (Colour online) Linking the structural response (*a*–*d*) with the wake patterns (*e*). The simulation results show the dislocation of the shed vortex tubes around IL nodes at $U_r = 17.22$, highlighting the ‘2S’ mode above the black dashed line and the ‘P+S’ mode below the black dashed line: (*a*) the IL and the CF amplitude response; (*b*) the PSD of the CF displacement; (*c*) the PSD of the CF flow velocity; (*d*) phase difference α of the CF flow velocity; (*e*) a series of snapshots of the vortex shedding over one period at $t = 0$, $t = \frac{1}{4}T$, $t = \frac{1}{2}T$, $t = \frac{3}{4}T$ and $t = T$ from left to right, where T is the vibration period at $U_r = 17.22$. The black dashed line marks location $z/d = -200$. Note that the CF flow velocity is taken at three diameters downstream from the mean IL displacement and the vortices are represented by isosurfaces of $Q = 0.1$ and coloured by ω_z.

circles denoting the time of the snapshots. At $z/d = -210$ for $U_r = 17.22$ in figure 20, C_{my} is a small negative value, as the subfigures (*f*) show that the fluctuating lift force of a small amplitude is in-phase with the acceleration. Subfigures (*a*) to (*e*) display a flow pattern as follows: at the bottom of the cylinder trajectory (subfigures *a*), one CCW vortex is about to detach from the cylinder rear, while a CW vortex forms in the upper shear layer. In subfigures (*b*), as the cylinder moves upwards, the CW vortex extends across the cylinder rear and pairs with the rolled-up CCW vortex in the wake. In subfigures (*c*), the cylinder then moves to the top of its oscillation where the CW vortex is stretched to split into two CW vortices. When the cylinder moves downwards in the second half-cycle of the oscillation (subfigures *d*), one of the two CW vortices moves together with the previously shed positive vortex, resulting in a vortex pair

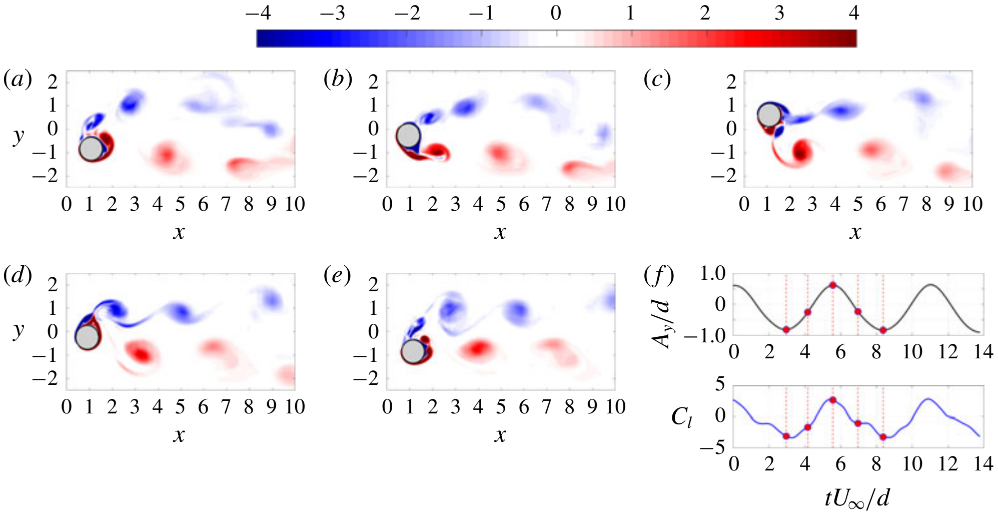

FIGURE 20. (Colour online) Simulation results of 2-D snapshots of the vortices at $z/d = -185$ for $U_r = 17.22$ over one period of CF oscillation: (*a–e*) instantaneous field of ω_z; (*f*) time trace of the cylinder CF motion (*a–c*) and the oscillating lift force (*d–f*). The red circle highlights the corresponding time from (*a*) to (*e*).

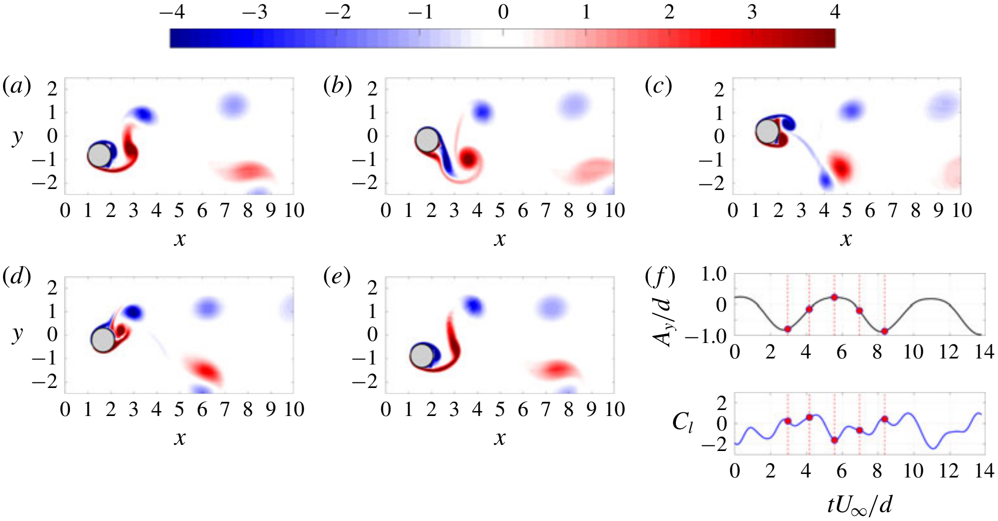

FIGURE 21. (Colour online) Simulation results of 2-D snapshots of the vortices at $z/d = -210$ for $U_r = 17.22$ over one period of CF oscillation: (*a–e*) instantaneous field of ω_z; (*f*) time trace of the cylinder CF motion (*a–c*) and the oscillating lift force (*d–f*). The red circle highlights the corresponding time from (*a*) to (*e*).

detaching from the cylinder in the lower half of the wake. In the meantime, the other CW vortex rolls up and is ready to detach from the cylinder in the upper half of the wake. This results in a shedding mode of ‘P+S’ (Williamson & Govardhan 2008). Meanwhile, at $z/d = -185$ for $U_r = 17.22$ in figure 21, C_{my} exhibits a large positive

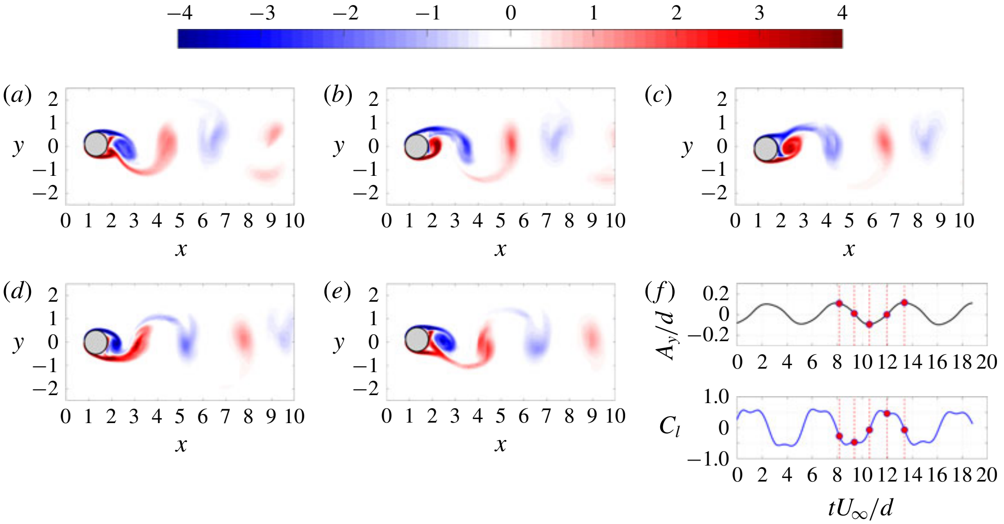

FIGURE 22. (Colour online) Simulation results of 2-D snapshots of the vortices at $z/d = -90$ for $U_r = 14.54$ over one period of CF oscillation: (*a*–*e*) instantaneous field of ω_z; (*f*) time trace of the cylinder CF motion (*a*–*c*) and the oscillating lift force (*d*–*f*). The red circle highlights the corresponding time from (*a*) to (*e*).

value, as the subfigures (*f*) show that the fluctuating lift force of a large amplitude is in anti-phase with acceleration. Subfigures (*a*) to (*e*) display a different flow pattern of a classical '2S' mode, compared to the 'P+S' mode found in the CW C_{my} region, as follows: at the bottom of the cylinder trajectory (subfigures *a*), one CW vortex is about to leave the cylinder in the upper half of the wake, while a CCW vortex forms on the upper half of the cylinder rear. In subfigures (*b*), as the cylinder moves upwards, the upper negative shear layer grows at the cylinder back and, in the meantime, the CCW vortex rolls up and is ready to detach. In subfigures (*c*), the cylinder then moves to its top of the oscillation where the CCW vortex moves downstream in the lower half of the wake. When the cylinder moves downwards in the second half-cycle of the oscillation (subfigures *d*), another CW vortex grows in strength in the upper half of the wake and then the whole process repeats from subfigures (*a*).

Comparing the vortex formation around the oscillating cylinder between the regions of $C_{my} < 0$ and $C_{my} > 0$, a clear difference can be seen in the timing of the vortex formation relative to the cylinder motion. Furthermore, it is found that for the positive C_{my} region with the '2S' mode, the shedding vortex forms close to the moving cylinder, compared to the negative C_{my} region with the 'P+S' mode, which is also observed in the CF-only rigid cylinder vibration of controlled trajectory by Carberry *et al.* (2005). Nonetheless, in order to thoroughly understand the coupling mechanism between the vortex shedding and cylinder vibration, more simulations and experiments of the rigid cylinder vibrating with controlled in-line and cross-flow coupled trajectories are needed, as well as more studies of the effect of the in-line motion on the forces and the wake patterns.

Furthermore, at $z/d = -90$ and $z/d = -145$ for $U_r = 14.54$ of the model group '5/3' figures 22(*a*–*e*) and 23(*a*–*e*) display a flow pattern of the classical '2S' mode, similar to the flow pattern in the region of large positive C_{my} for $U_r = 17.22$. However, at $U_r = 14.54$, the vortices no longer form at the upper- or lower-half side of the

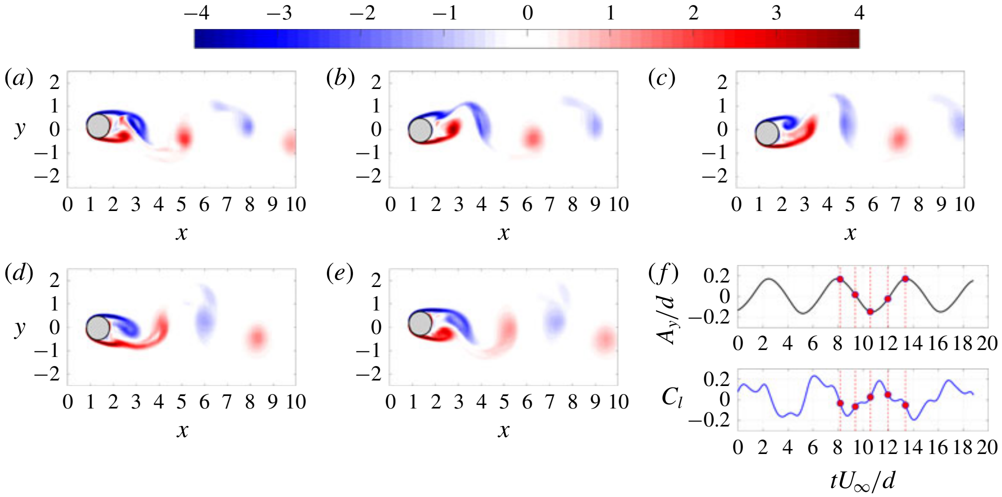

FIGURE 23. (Colour online) Simulation results of 2-D snapshots of the vortices at $z/d=-145$ for $U_r=14.54$ over one period of CF oscillation: (*a–e*) instantaneous field of ω_z; (*f*) time trace of the cylinder CF motion (*a–c*) and the oscillating lift force (*d–f*). The red circle highlights the corresponding time from (*a*) to (*e*).

cylinder, instead they appear directly at the rear of the cylinder, close to the centre line of the cylinder CF oscillation. As a result, the cylinder wake is narrower with the cores of the alternating CCW and CW vortices aligned with the centre line of the cylinder CF motion. In contrast, in figure 20 of '2S' vortex mode, CCW and CW vortices distinctively occupy the upper- and lower-half of the wake, which leads to a wider wake.

5. Conclusion

We studied experimentally and numerically the vortex-induced vibrations of a long flexible cylinder in uniform flow over a wide range of reduced velocity, aiming at answering key questions for flexible cylinder VIV prediction namely: what is the relation between the hydrodynamic data for a rigid cylinder versus those for a flexible model, and what is the role of the variable added mass coefficients. Based on a comparison between the hydrodynamic coefficients measured through rigid cylinder forced oscillation at $Re=5\,715$, and the sectional fluid coefficients reconstructed from the flexible cylinder vibration at Re in the range of $250--2\,300$, we conclude that a rigid cylinder undergoing the same prescribed cross-flow and in-line motion as a section of the flexible cylinder, can predict the sectional hydrodynamic coefficients at that location accurately. Furthermore, by studying the extensive hydrodynamic database constructed via rigid cylinder forced oscillation, we elucidate some of the complex physics behind the flexible cylinder VIV in uniform flow, as follows.

The phase θ between cross-flow and in-line response has a strong influence on the hydrodynamic coefficients for both rigid and flexible cylinders.

The lift coefficient in-phase with the velocity C_{lv} along the oscillating flexible cylinder is found to be strongly correlated with the phase θ. The positive C_{lv} region, where energy is transferred from the fluid to the structure, favours a phase of $\theta\in[0,\,\pi]$ corresponding to counter-clockwise IL and CF trajectories. In addition, the cylinder vibration amplitude and the true reduced velocity are key factors affecting C_{lv}. As the reduced velocity is increased while the flexible cylinder vibrates at the same cross-flow mode, an asymmetric amplitude response appears along the span containing a mixture of standing and travelling waves. Positive C_{lv} of large magnitude is found in locations with small cross-flow amplitude and counter-clockwise phase distribution, while a vibration of large amplitude damps out the energy transferring it from the structure to the fluid.

The added mass coefficient in the cross-flow direction C_{my} varies significantly along the flexible cylinder due to the effect of the phase θ distribution along the span; a similar change of C_{my} as a function of the phase angle was found also in rigid cylinder experiments (Dahl 2008). At two different reduced velocities, the C_{my} distribution may be significantly different, adjusting the system's true natural frequency in the cross-flow direction in order to match the vortex shedding frequency.

The added mass coefficient in the in-line direction C_{mx} is found to have a smaller variation along the flexible cylinder and as a function of the reduced velocity, compared to C_{my}. However, the span-averaged C_{mx} and C_{my} are interrelated, in order to reach a dual resonance in both the in-line and the cross-flow directions.

Identifying the wake patterns behind an oscillating flexible cylinder is essential to explain the form of the hydrodynamic coefficient distribution and predict the structural response of the system. Using LES, we found that in the wake of the oscillating flexible cylinder in uniform flow, vortices shed spanwise in cells defined between adjacent IL nodes; continuous vortex tubes dislocate in space at IL nodes, while the interesting phenomenon of a 'void' vortex shedding region is observed at a CF node provided the same point is not also an IL node. Hence, the IL motion changes in phasing along the span can affect the cross-flow vibration due to different timing of the vortex formation as well changes in the vortex shedding mode. In particular, a negative cross-flow added mass coefficient C_{my} is strongly correlated with the vortex shedding mode 'P+S'.

Acknowledgements

The authors acknowledge with gratitude support from Chevron Energy Technology Company and BP Exploration Operating Company Limited. The authors would like to acknowledge one of the referees for the insightful comments on the three-dimensional vortical structure behind the flexible cylinder which helps to greatly improve the quality of the paper.

Appendix A. Underwater optical measurement system

In current experiments, the underwater optical measurement system uses sports cameras 'GoPro Hero 4 Black', the technical details of which can be found in GoPro (2014). The camera resolution calibration is performed in the water for the mode '240 FPS + 720 p' (the sampling rate is 240 Hz and the frame size is 1280 × 720 pixel), and the following equation of the resolution per pixel (R) as a function of the distance between camera and cylinder (x) centre is found:

$$R = A + Bx, \tag{A 1}$$

where x is the distance between the camera and cylinder centre in units of cm, A is found to be 0.0009, B is found to be 0.003961 and R is the resolution per pixel in units of mm pixel^{-1}. For the entire measurement system, three cameras are

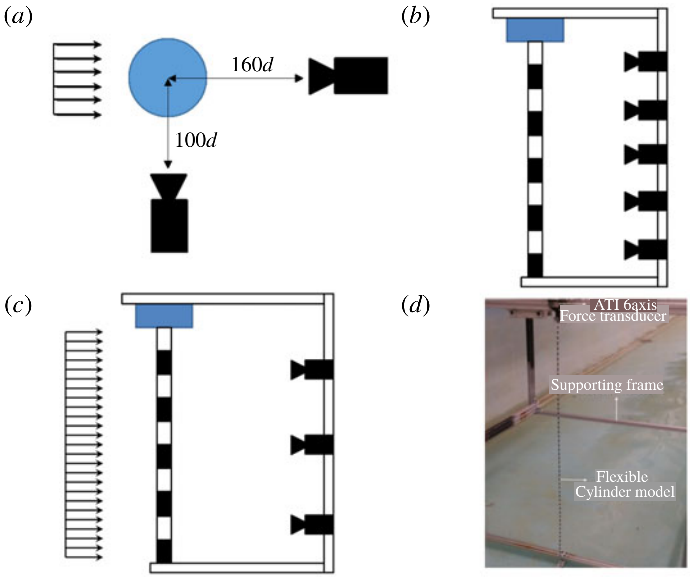

FIGURE 24. (Colour online) Schematic and photograph of the flexible cylinder experiment set-up in the tow tank: (*a*) top view of downstream and side cameras $160d$ and $100d$ away from the centre of the model; (*b*) front view of five cameras downstream of the model; (*c*) side view of three cameras on the side of the model; (*c*) photo, the actual set-up of the flexible model on the supporting frame in the tow tank.

installed over $160d$ downstream of the model and five cameras are installed $100d$ beside the model to measure CF and IL vibrations, respectively, along the entire flexible cylinder, shown in figure 24. Taking one of the cameras downstream of the model as an example, the resolution per pixel of the camera for the model plane is 0.3178 mm pixel^{-1}, which means that one diameter of the cylinder $d = 5$ mm has 15.74 pixels.

In order to capture and follow the trajectory of the white and black markers, a code for image processing and motion tracking has been developed (Fan & Triantafyllou 2017), which follows the general protocol of the motion-based multiple object tracking method (Moeslund & Granum 2001). The key steps of image processing are shown in the flowchart of figure 25. For each camera, in the rest step, an appropriate colour threshold is selected to convert colour images into binary frames. Second, via blob analysis, the centroids and the bounding boxes of the objects will be detected in the current frame, and then the track prediction/assignment subroutine is executed. To follow the object accurately, noise must be reduced. Based on the Euclidean distance between the assigned track location of the current frame and the Kalman filter predicted track location, it will decide whether to update the track position or delete the track as it is viewed as noise. Furthermore, the eight cameras are synchronized by the background lighting before running the each experiment. To this end, four 1500-lumen underwater lights will be switched on, creating a one video frame for each camera with a sharp contrast background lighting as the synchronization signal. Last, the calibration is applied on the measured marker movement in units of pixels to the dimensionless vibration amplitude along the model.

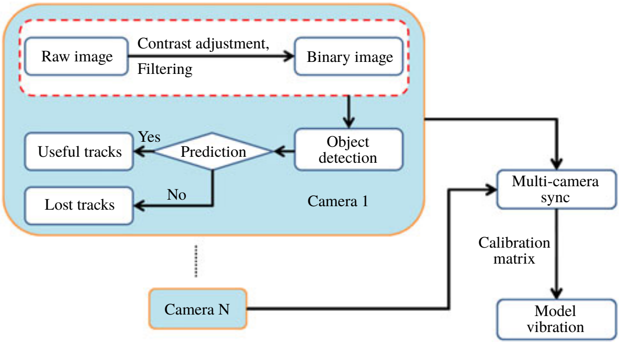

FIGURE 25. (Colour online) Flowchart of the imaging process and motion track method for underwater optical measurement system with multiple cameras.

Appendix B. Inverse vortex force/coefficients in the experiment

Neglecting the bending stiffness contribution, the flexible cylinder can be modelled as a taut string subject to distributed external forces, described by the following equation:

$$\mu\frac{\partial^2 u(x,t)}{\partial t^2}-\frac{\partial}{\partial x}\left(T\frac{\partial u(x,t)}{\partial x}\right)+\beta\frac{\partial u(x,t)}{\partial t}=F(x,t), \tag{B 1}$$

where μ is the structural mass per unit length (without hydrodynamic added mass), T is the model tension, β is the structural damping, $u(x,t)$ is the displacement in either the IL or the CF direction and $F(x,t)$ is the external hydrodynamic force per unit length on the model. With the dense temporal and spatial measurement of the model displacement in the IL and the CF directions, we are able to inversely calculate the vortex force F_i^j exerted on the model node j at time t_i directly, as follows:

$$F_i^j=\mu\frac{u_{i+1}^j+u_{i-1}^j-2u_i^j}{\Delta t^2}-T^j\frac{u_i^{j+1}+u_i^{j-1}-2u_i^j}{\Delta x^2}+\beta\frac{u_{i+1}^j-u_{i-1}^j}{2\Delta t}. \tag{B 2}$$

In the current experiment, the string model was clamped at both ends with boundary conditions $u^0=u^n=0$. Therefore, the fluctuating non-dimensional hydrodynamic coefficient at different locations along the model is calculated as follows:

$$\tilde{C}(j,t)=\frac{F_i^j-\dfrac{1}{n}\displaystyle\sum_{i=1}^{n}F_i^j}{0.5\rho U^2 d}, \tag{B 3}$$

where ρ is the fluid density and U is the towing speed for each experiment case.

The force coefficient in-phase with the velocity C_v, the force coefficient in-phase with the acceleration C_a, and the added mass coefficient C_m in either the IL or the CF direction at location j along the model can be calculated as follows:

$$C_v(j)=\frac{\dfrac{2}{T_s}\displaystyle\int_{T_s}(\tilde{C}(j,t)\dot{\tilde{\xi}}(j,t))\,\mathrm{d}t}{\sqrt{\dfrac{2}{T_s}\displaystyle\int_{T_s}(\dot{\tilde{\xi}}^2(j,t))\,\mathrm{d}t}}, \tag{B 4}$$

$$C_a(j) = \frac{\dfrac{2}{T_s}\displaystyle\int_{T_s} (\tilde{C}(j,t)\ddot{\tilde{\xi}}(j,t))\,\mathrm{d}t}{\sqrt{\dfrac{2}{T_s}\displaystyle\int_{T_s} (\ddot{\tilde{\xi}}^2(j,t))\,\mathrm{d}t}}, \tag{B 5}$$

$$C_m(j) = -\frac{2U^2}{\pi d^2}\cdot\frac{\displaystyle\int_{T_s} (\tilde{C}(j,t)\ddot{\tilde{\xi}}(j,t))\,\mathrm{d}t}{\displaystyle\int_{T_s} (\ddot{\tilde{\xi}}^2(j,t))\,\mathrm{d}t}, \tag{B 6}$$

where $\tilde{\xi}$ is the IL or the CF displacement non-dimensionalized by the model diameter d, and $\dot{\tilde{\xi}}$ and $\ddot{\tilde{\xi}}$ are the first and second derivatives of ξ with respect to time, namely the non-dimensional velocity and acceleration.

Appendix C. Predicted true natural frequency

Using the mean tension $\overline{T}$ along the flexible cylinder and spatial average added mass per unit length in either the IL or the CF direction $\overline{\mu_x}$ and $\overline{\mu_y}$, the predicted modal natural frequencies in either the IL or the CF direction $\overline{f_{nx}^{true}}$ and $\overline{f_{ny}^{true}}$ are given by the following equation (C 1):

$$\left.\begin{aligned} \overline{f_{nx}^{true}} &= \frac{n}{2L}\sqrt{\frac{\overline{T}}{\mu+\overline{\mu_x}}}, \\ \overline{f_{ny}^{true}} &= \frac{m}{2L}\sqrt{\frac{\overline{T}}{\mu+\overline{\mu_y}}}, \end{aligned}\right\} \tag{C 1}$$

Taking into consideration the non-uniform added mass C_m and tension T distribution, based on the string vibration equation (B 1), we can form the following mass matrix $\boldsymbol{M}$ with n nodes:

$$\boldsymbol{M} = \begin{bmatrix} \mu+\mu_{x/y}^{(2)} & 0 & \dots & 0 \\ 0 & \mu+\mu_{x/y}^{(3)} & \dots & 0 \\ \vdots & & \ddots & 0 \\ 0 & \dots & 0 & \mu+\mu_{x/y}^{(n-1)} \end{bmatrix}, \tag{C 2}$$

where $\mu_{x/y}^{(j)}$ is the added mass per unit length in either the IL or the CF direction at node j. We can also form the following stiffness matrix $\boldsymbol{K}$:

$$\boldsymbol{K} = \frac{1}{\Delta x^2}\begin{bmatrix} 2T^{(2)} & -T^{(3)} & \dots & 0 \\ -T^{(2)} & 2T^{(3)} & \dots & 0 \\ \vdots & & \ddots & -T^{(n-1)} \\ 0 & \dots & -T^{(n-2)} & 2T^{(n-1)} \end{bmatrix}, \tag{C 3}$$

where $T^{(j)}$ is the tension at node j.

We can then acquire the corresponding eigenvalues of the system, namely the predicted true modal natural frequency without damping f_n^{true}. In figure 26, we

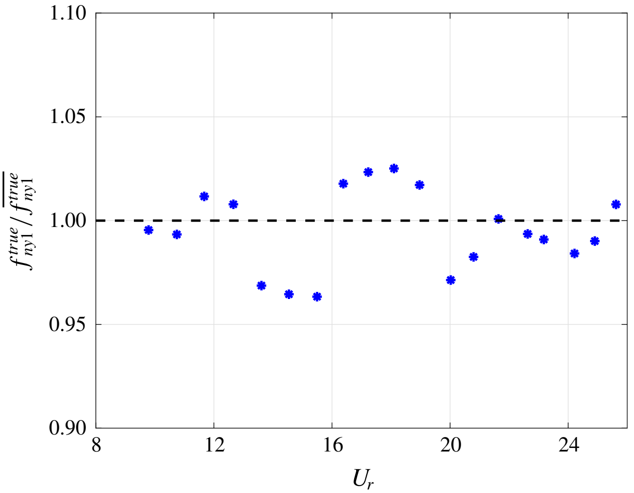

FIGURE 26. (Colour online) Ratio between f^{true}_{ny1} and $\overline{f^{true}_{ny1}}$ over various reduced velocity U_r. The difference between f^{true}_{ny1} and $\overline{f^{true}_{ny1}}$ is less than 5 %.

plot the ratio between the predicted true 1st modal natural frequency in the CF direction f^{true}_{ny1} and the predicted 1st modal natural frequency in the CF direction $\overline{f^{true}_{ny1}}$ over different reduced velocities, and it shows that the difference between the two predictions is less than 5 %. Hence, we can conclude that the predicted modal natural frequency $\overline{f^{true}_{n}}$ based on the spatial average added mass and mean tension along the span is a good representative for the predicted true modal natural frequency in the current experiment.

Appendix D. Hydrodynamic coefficients of the rigid cylinder in forced vibration

We have conducted extensive experiments for the rigid cylinder subject to forced vibrations in uniform inflow with prescribed IL and CF motions. We combined these new results with previous experimental results by Dahl (2008) and Zheng *et al.* (2014*a*) to construct a hydrodynamic database for rigid cylinder VIV of coupled IL and CF vibrations. In this section, we present some of these results of hydrodynamic coefficients in order to quantify the general trend of the fluid forces of the rigid cylinder undergoing IL and CF coupled oscillations.

D.1. *The lift coefficient in-phase with the velocity* C_{lv}

The lift coefficient in-phase with the velocity C_{lv} describes the energy transfer between the structure and the fluid: when C_{lv} is larger than zero, positive energy is transferred from the fluid to the structure, and, on the other hand, when C_{lv} is negative, the fluid helps the structure to dissipate energy.

Figure 27 shows C_{lv} contours as a function of A_x/d and A_y/d for the selected V_r and θ from rigid cylinder forced vibration experiments. Comparing between figures 27(*a*) and 27(*b*), we see that C_{lv} is largely negative for clockwise motion, while it is positive at small A_y/d for counter-clockwise motion. Furthermore, in general C_{lv} decreases with increasing A_y/d and A_x/d. In addition, shown in figures 27(*b*) and 27(*d*) for

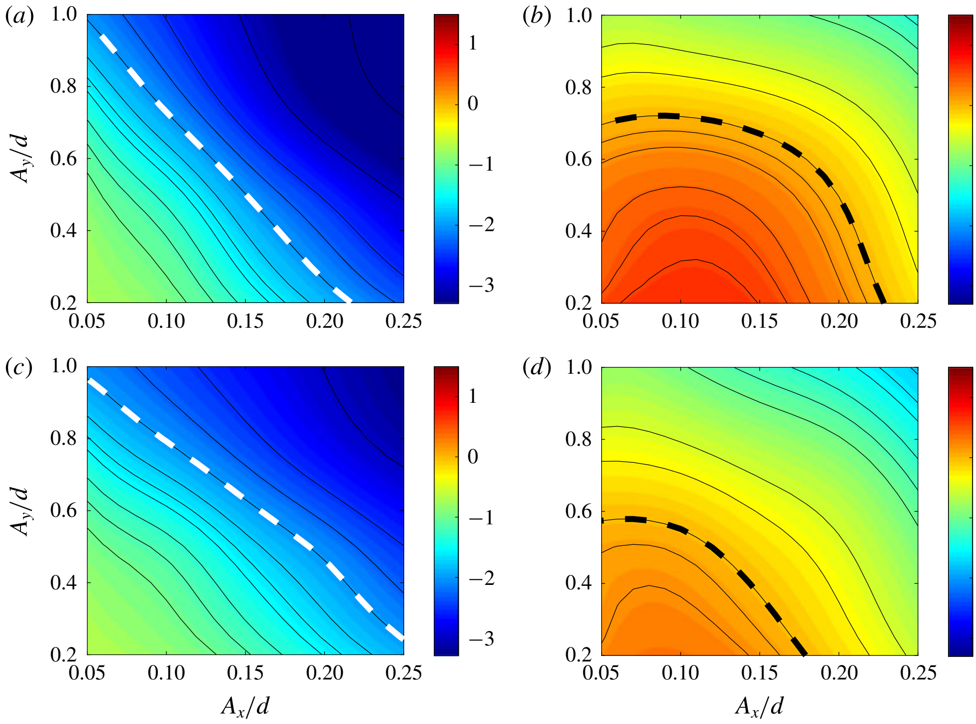

FIGURE 27. (Colour online) Contours of the lift coefficient in-phase with the velocity as a function of A_x/d and A_y/d from the hydrodynamic coefficient database: (*a*) here $V_r = 5.5$ and $\theta = 3\pi/2$; (*b*) $V_r = 5.5$ and $\theta = \pi/2$; (*c*) $V_r = 4.75$ and $\theta = 3\pi/2$; (*d*) $V_r = 4.75$ and $\theta = \pi/2$. Bold black dashed line highlights the contour line of $C_{lv} = 0$, and bold white dashed line highlights the contour line of $C_{lv} = -2$.

CCW trajectories, as V_r increases from 4.75 to 5.5 (namely the reduced frequency f_r decreases from 0.21 to 0.18), the positive area of C_{lv} gets larger. By examining figures 27(*a*) and 27(*c*), as V_r decreases from 5.5 to 4.75, generally the magnitude of negative C_{lv} decreases as well, indicated by the $C_{lv} = -2$ contour line.

D.2. *The added mass coefficient in the CF direction C_{my} and in the IL direction C_{mx}*

Due to the change of the relative timing between the cylinder motion and shedding vortex, the true added mass coefficient of the cylinder may vary significantly during the vortex-induced vibration. Figure 28 shows sample contours of the CF added mass coefficient C_{my} as a function of V_r and θ from the forced vibration experiment on rigid cylinders for three different A_x/d and A_y/d combinations. We find that C_{my} for the coupled IL and CF vibration is strongly dependent not only on V_r but also on θ. We note that:

(i) With increasing V_r, the area where C_{my} is negative becomes larger (the bold black dashed line highlights the contour line of $C_{my} = 0$).

(ii) Negative values of C_{my} are associated with θ values between $\pi/2$ and $3\pi/2$.

(iii) The C_{my} has a minimum value around $V_r = 7$ and $\theta = \pi$.

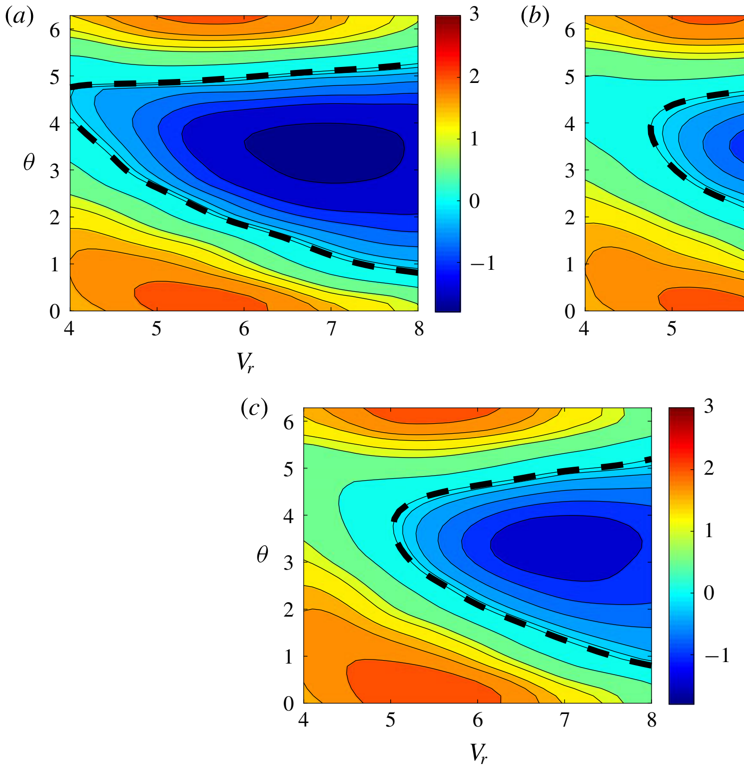

FIGURE 28. (Colour online) Contours of the added mass coefficient in the CF direction as a function of V_r and θ from the hydrodynamic coefficient database: (*a*) here $A_x/d = 0.15$ and $A_y/d = 0.80$; (*b*) $A_x/d = 0.10$ and $A_y/d = 0.80$; (*c*) $A_x/d = 0.10$ and $A_y/d = 0.50$. The bold black dashed line highlights the contour line of $C_{my} = 0$.

In contrast to the effects of the reduced velocity and phase angle, as shown in figures 28(*b*) and 28(*c*), the CF amplitude has a very weak influence on C_{my}. Figures 28(*a*) and 28(*b*) shows that the area with negative C_{my} increases slightly with increasing A_x/d. Figure 29 shows the contours of the IL added mass coefficient C_{mx} as a function of V_r and θ from the forced vibration experiment on rigid cylinders. The same as C_{my}, C_{mx} strongly depends on V_r and θ, while the effect of A_x/d and A_y/d is weak. Overall, C_{mx} varies more gently than C_{my}.

Appendix E. Comparison between the simulations and experiments

In this section, we present the numerical simulation results and compare them with the corresponding flexible cylinder experiments on the frequency and displacement response.

We performed eight simulations with U_r from 10.75 to 17.22, covering the modal group 4/2, 5/3 and 6/3. The simulation parameters in terms of mass ratio, aspect ratio, structural damping ratio, Reynolds number and reduced velocity match with those of the experiment well. Note that in the simulation the tension along the flexible model is constant, while in the experiment the tension along the flexible

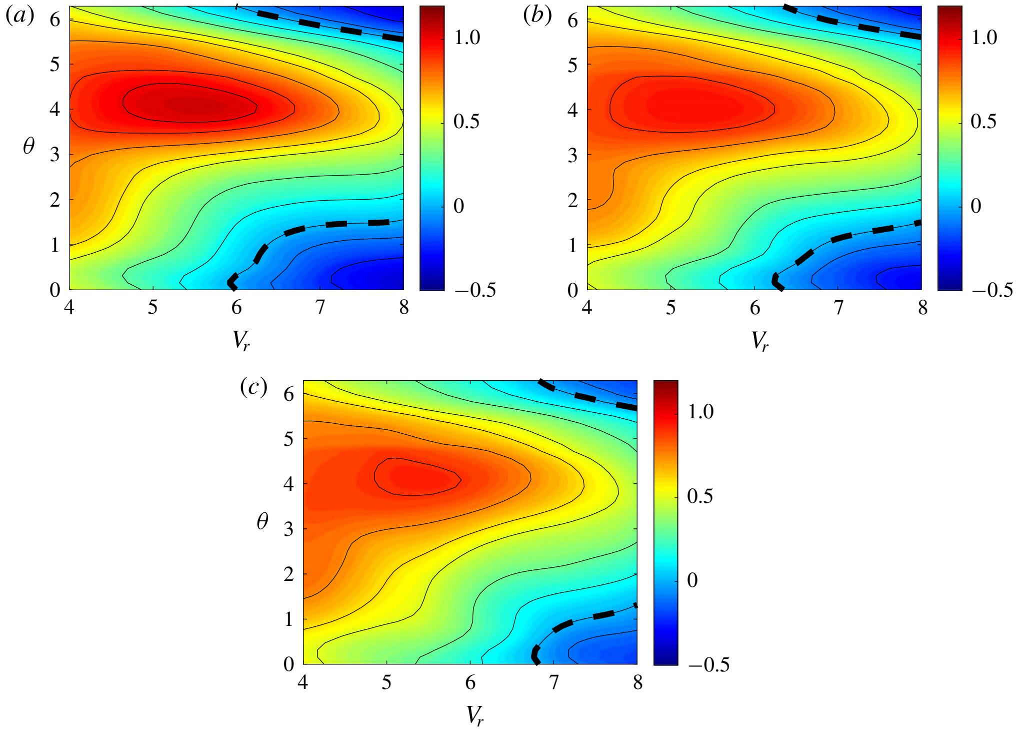

FIGURE 29. (Colour online) Contours of the added mass coefficient in the IL direction as a function of V_r and θ from the hydrodynamic coefficient database: (*a*) here $A_x/d=0.15$ and $A_y/d=0.80$; (*b*) $A_x/d=0.10$ and $A_y/d=0.80$; (*c*) $A_x/d=0.10$ and $A_y/d=0.50$. The bold black dashed line highlights the contour line of $C_{mx}=0$.

model linearly varies due to the gravity effect. Such difference will indeed affect the modal shape of the displacement response. However, from the simulation result, we observe that the main phenomenon of the modal group switch agrees well with the experiment.

The frequency and the 1/10th highest peak of the displacement response in both the IL and the CF directions are shown in figure 30 at $U_r=12.66$ and figure 31 at $U_r=14.54$. The simulation result here shows that the model responds in a narrow-band single frequency pattern in the CF direction, while in the IL direction a dominating 2nd harmonics exists. The corresponding experimental displacement response at the same reduced velocity U_r is plotted in the subfigures (*b*,*d*) of figures 30 and 31. The simulation can reproduce accurately the modal group switch as that in the experiment, e.g. the modal group 4/2 at $U_r=12.66$ and the modal group 5/3 at $U_r=14.54$. In figures 32 and 33, we plot the 1/10th highest peak of the displacement response in the IL and the CF directions for both the simulation (red) and the experiment (blue). The simulation prediction agrees well with the experiment.

The maximum of the 1/10th highest peak of the displacement response in the IL and the CF directions along the span is plotted in figure 34, together with the non-dimensional frequency response (the blue dot represents the experiment, and the red circle denotes the simulation). The results here show that the simulation reproduces

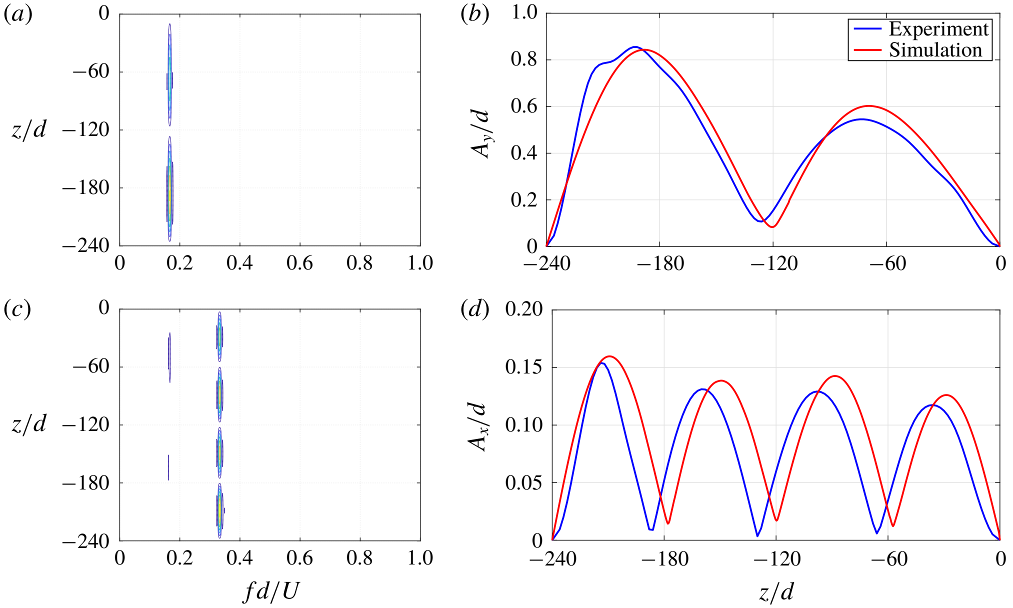

FIGURE 30. (Colour online) Comparison between the simulation and the experiment on the displacement response at $U_r = 12.66$: (*a*) the CF frequency response; (*b*) the CF displacement response; (*c*) the IL frequency response; (*d*) the IL displacement response.

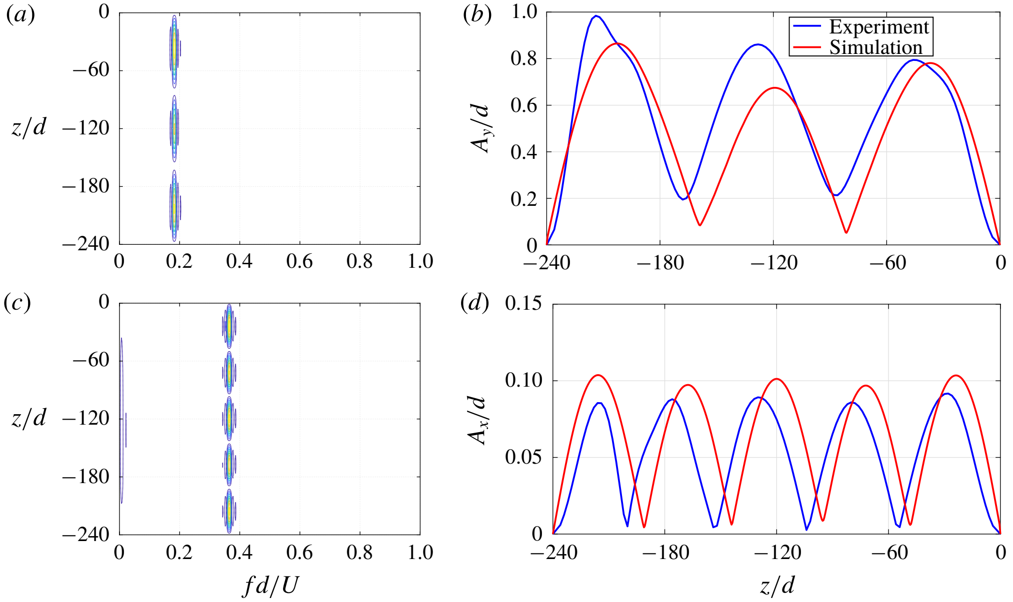

FIGURE 31. (Colour online) Comparison between the simulation and the experiment on the displacement response at $U_r = 14.54$: (*a*) the CF frequency response; (*b*) the CF displacement response; (*c*) the IL frequency response; (*d*) the IL displacement response.

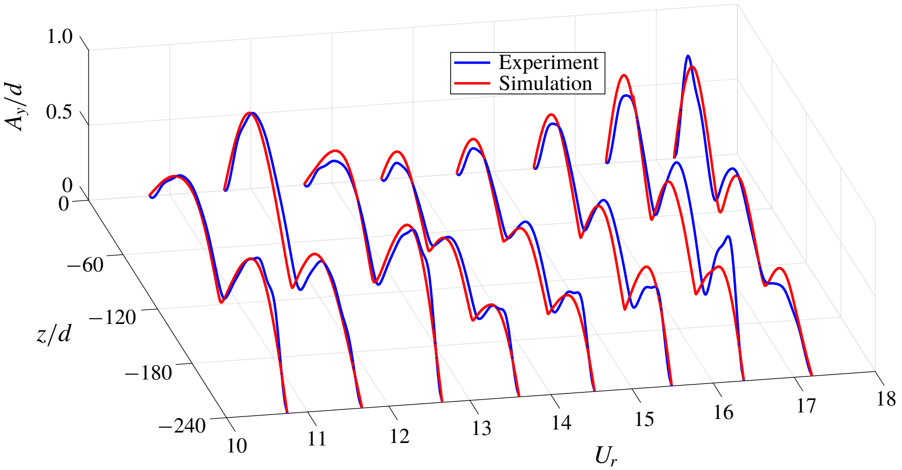

FIGURE 32. (Colour online) Comparison between the simulation and the experiment on the CF displacement response from $U_r = 10.75$ to $U_r = 17.22$.

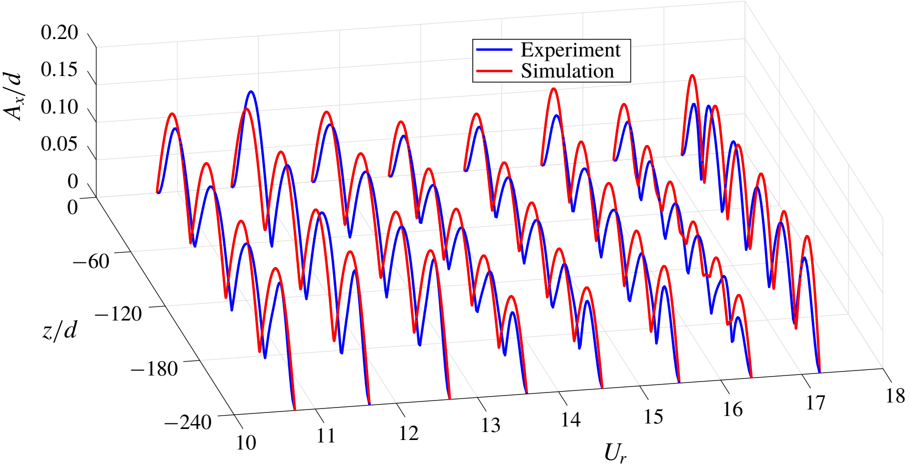

FIGURE 33. (Colour online) Comparison between the simulation and the experiment on the IL displacement response from $U_r = 10.75$ to $U_r = 17.22$.

the phenomena of the increasing displacement response in the same modal group as well as the displacement and frequency response jump between the different modal groups. In addition, note that at $U_r = 13.61$, the simulation result of frequency and displacement is different from the different initial conditions starting from either $U_r = 12.66$ or $U_r = 14.54$, which shows an interesting hysteresis phenomenon between the modal group switch of the flexible cylinder.

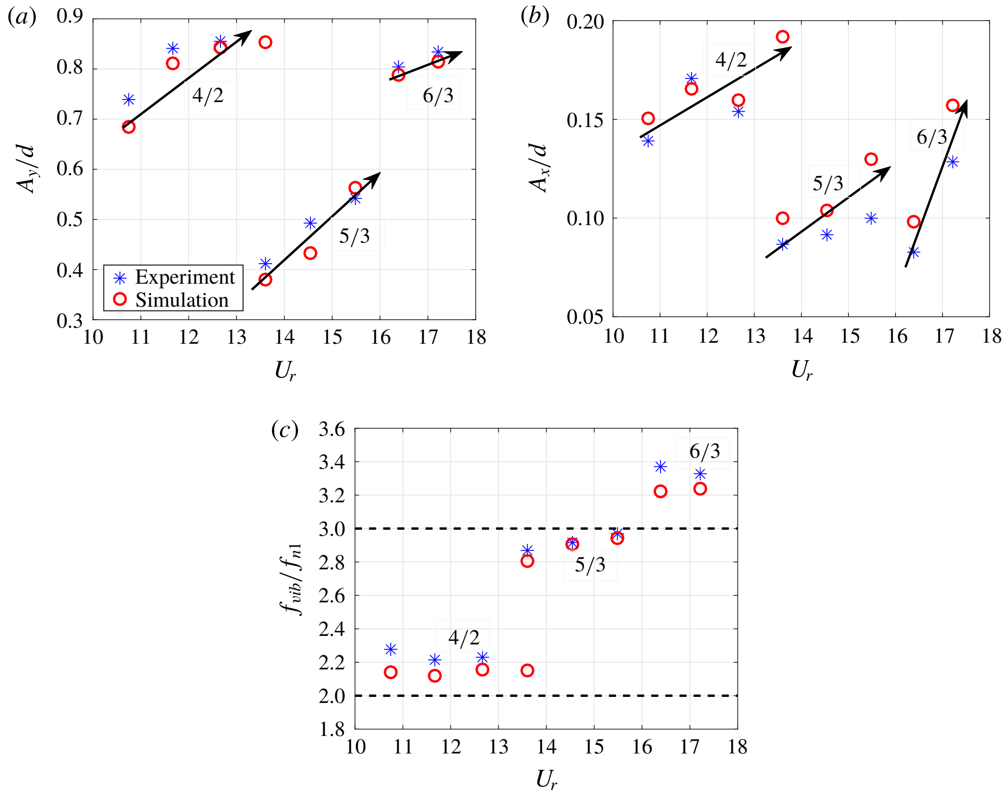

FIGURE 34. (Colour online) Comparison between the simulation and the experiment from $U_r = 10.75$ to $U_r = 17.22$: (*a*) the maximum of CF displacement response; (*b*) the maximum of CF displacement response; (*c*) the non-dimensional frequency response in the CF direction.

REFERENCES

ARONSEN, K. H. 2007 An experimental investigation of in-line and combined in-line and cross-flow vortex induced vibrations. PhD thesis, Norwegian University of Science and Technology.

BANGASH, Z. A. & HUERA-HUARTE, F. J. 2015 On the flow around the node to anti-node transition of a flexible cylinder undergoing vortex-induced vibrations. *Phys. Fluids* **27** (6), 065112.

BEARMAN, P. W. 1984 Vortex shedding from oscillating bluff bodies. *Annu. Rev. Fluid Mech.* **16** (1), 195–222.

BEARMAN, P. W. 2011 Circular cylinder wakes and vortex-induced vibrations. *J. Fluids Struct.* **27** (5-6), 648–658.

BISHOP, R. E. D. & HASSAN, A. Y. 1964 The lift and drag forces on a circular cylinder oscillating in a flowing fluid. *Proc. R. Soc. Lond.* A **277** (1368), 51–75.

BOURGUET, R., KARNIADAKIS, G. E. & TRIANTAFYLLOU, M. S. 2013 Phasing mechanisms between the in-line and cross-flow vortex-induced vibrations of a long tensioned beam in shear flow. *Comput. Struct.* **122**, 155–163.

BOURGUET, R., MODARRES-SADEGHI, Y., KARNIADAKIS, G. E. & TRIANTAFYLLOU, M. S. 2011 Wake-body resonance of long flexible structures is dominated by counterclockwise orbits. *Phys. Rev. Lett.* **107** (13), 134502.

BRAATEN, H. & LIE, H. 2004 NDP riser high mode VIV tests. *Tech. Rep.* (512394.00), 01. Norwegian Marine Technology Research Institute.

BRIKA, D. & LANEVILLE, A. 1993 Vortex-induced vibrations of a long flexible circular cylinder. *J. Fluid Mech.* **250**, 481–508.

CARBERRY, J., SHERIDAN, J. & ROCKWELL, D. 2005 Controlled oscillations of a cylinder: forces and wake modes. *J. Fluid Mech.* **538**, 31–69.

CHAPLIN, J. R., BEARMAN, P. W., CHENG, Y., FONTAINE, E., GRAHAM, J. M. R., HERFJORD, K., HUERA-HUARTE, F. J., ISHERWOOD, M., LAMBRAKOS, K., LARSEN, C. M. *et al.* 2005*a* Blind predictions of laboratory measurements of vortex-induced vibrations of a tension riser. *J. Fluids Struct.* **21** (1), 25–40.

CHAPLIN, J. R., BEARMAN, P. W., HUERA-HUARTE, F. J. & PATTENDEN, R. J. 2005*b* Laboratory measurements of vortex-induced vibrations of a vertical tension riser in a stepped current. *J. Fluids Struct.* **21** (1), 3–24.

DAHL, J. M. 2008 Vortex-induced vibration of a circular cylinder with combined in-line and cross-flow motion. PhD thesis, Massachusetts Institute of Technology, Cambridge, MA.

DAHL, J. M., HOVER, F. S. & TRIANTAFYLLOU, M. S. 2006 Two-degree-of-freedom vortex-induced vibrations using a force assisted apparatus. *J. Fluids Struct.* **22** (6), 807–818.

DAHL, J. M., HOVER, F. S. & TRIANTAFYLLOU, M. S. 2008 High harmonic forces and predicted vibrations from forced in-line and cross-flow cylinder motions. In *The 18th International Offshore and Polar Engineering Conference*. International Society of Offshore and Polar Engineers.

DAHL, J. M., HOVER, F. S., TRIANTAFYLLOU, M. S., DONG, S. & KARNIADAKIS, G. E. 2007 Resonant vibrations of bluff bodies cause multivortex shedding and high frequency forces. *Phys. Rev. Lett.* **99** (14), 144503.

DAHL, J. M., HOVER, F. S., TRIANTAFYLLOU, M. S. & OAKLEY, O. H. 2010 Dual resonance in vortex-induced vibrations at subcritical and supercritical Reynolds numbers. *J. Fluid Mech.* **643**, 395–424.

DU, L., JING, X. & SUN, X. 2014 Modes of vortex formation and transition to three-dimensionality in the wake of a freely vibrating cylinder. *J. Fluids Struct.* **49**, 554–573.

EVANGELINOS, C. & KARNIADAKIS, G. E. 1999 Dynamics and flow structures in the turbulent wake of rigid and flexible cylinders subject to vortex-induced vibrations. *J. Fluid Mech.* **400**, 91–124.

EVANGELINOS, C., LUCOR, D. & KARNIADAKIS, G. E. 2000 DNS-derived force distribution on flexible cylinders subject to vortex-induced vibration. *J. Fluids Struct.* **14** (3), 429–440.

FACCHINETTI, M. L., DE LANGRE, E. & BIOLLEY, F. 2004 Coupling of structure and wake oscillators in vortex-induced vibrations. *J. Fluids Struct.* **19** (2), 123–140.

FAN, D., DU, H. & TRIANTAFYLLOU, M. S. 2016 Optical tracking measurement on vortex-induced vibration of flexible riser with short-length buoyance module. In *APS Fluid Dyn. Meeting Abstr.* American Physical Society.

FAN, D. & TRIANTAFYLLOU, M. S. 2017 Vortex-induced vibration of riser with low span to diameter ratio buoyancy modules. In *The 27th International Offshore and Polar Engineering Conference*. International Society of Offshore and Polar Engineers.

GABBAI, R. D. & BENAROYA, H. 2005 An overview of modeling and experiments of vortex-induced vibration of circular cylinders. *J. Sound Vib.* **282** (3-5), 575–616.

GILBERT, S. & SIGURDSON, L. 2010 The void structure in the wake of a self-oscillating flexible circular cylinder. *Exp. Fluids* **48** (3), 461–471.

GOPALKRISHNAN, R. 1993 Vortex-induced forces on oscillating bluff cylinders. PhD thesis, Massachusetts Institute of Technology, Cambridge, MA.

GOPRO INC. 2014 User manual: GoPro HERO 4 black.

GOVARDHAN, R. & WILLIAMSON, C. H. K. 2000 Modes of vortex formation and frequency response of a freely vibrating cylinder. *J. Fluid Mech.* **420**, 85–130.

GOVARDHAN, R. N. & WILLIAMSON, C. H. K. 2006 Defining the modified Griffin plot in vortex-induced vibration: revealing the effect of Reynolds number using controlled damping. *J. Fluid Mech.* **561**, 147–180.

GUERMOND, J.-L., PASQUETTI, R. & POPOV, B. 2011*a* Entropy viscosity method for nonlinear conservation law. *J. Comput. Phys.* **230** (11), 4248–4267.

GUERMOND, J.-L., PASQUETTI, R. & POPOV, B. 2011*b* From suitable weak solutions to entropy viscosity. *J. Sci. Comput.* **49** (1), 35–50.

HAN, Q., MA, Y., XU, W., FAN, D. & WANG, E. 2018 Hydrodynamic characteristics of an inclined slender flexible cylinder subjected to vortex-induced vibration. *Inter. J. Mech. Sci.* **148**, 352–365.

HUERA-HUARTE, F. J. & BEARMAN, P. W. 2009*a* Wake structures and vortex-induced vibrations of a long flexible cylinder part 1: dynamic response. *J. Fluids Struct.* **25** (6), 969–990.

HUERA-HUARTE, F. J. & BEARMAN, P. W. 2009*b* Wake structures and vortex-induced vibrations of a long flexible cylinder part 2: drag coefficients and vortex modes. *J. Fluids Struct.* **25** (6), 991–1006.

HUERA-HUARTE, F. J., BEARMAN, P. W. & CHAPLIN, J. R. 2006 On the force distribution along the axis of a flexible circular cylinder undergoing multi-mode vortex-induced vibrations. *J. Fluids Struct.* **22** (6), 897–903.

JAUVTIS, N. & WILLIAMSON, C. H. K. 2003 Vortex-induced vibration of a cylinder with two degrees of freedom. *J. Fluids Struct.* **17** (7), 1035–1042.

JAUVTIS, N. & WILLIAMSON, C. H. K. 2004 The effect of two degrees of freedom on vortex-induced vibration at low mass and damping. *J. Fluid Mech.* **509**, 23–62.

KARNIADAKIS, G. E. & SHERWIN, S. 2005 *Spectral/hp Element Methods for Computational Fluid Dynamics*, 2nd edn. Oxford University Press.

KHALAK, A. & WILLIAMSON, C. H. K. 1999 Motions, forces and mode transitions in vortex-induced vibrations at low mass-damping. *J. Fluids Struct.* **13** (7–8), 813–851.

LARSEN, C. M., VIKESTAD, K., YTTERVIK, R., PASSANO, E. & BAARHOLM, G. S. 2001 *Vivana Theory Manual*. Marintek.

MODARRES-SADEGHI, Y., CHASPARIS, F., TRIANTAFYLLOU, M. S., TOGNARELLI, M. & BEYNET, P. 2011 Chaotic response is a generic feature of vortex-induced vibrations of flexible risers. *J. Sound Vib.* **330** (11), 2565–2579.

MODARRES-SADEGHI, Y., MUKUNDAN, H., DAHL, J. M., HOVER, F. S. & TRIANTAFYLLOU, M. S. 2010 The effect of higher harmonic forces on fatigue life of marine risers. *J. Sound Vib.* **329** (1), 43–55.

MOESLUND, T. B. & GRANUM, E. 2001 A survey of computer vision-based human motion capture. *Comput. Vis. Image. Underst.* **81** (3), 231–268.

NEWMAN, D. J. & KARNIADAKIS, G. E. 1996 Simulations of flow over a flexible cable: a comparison of forced and flow-induced vibration. *J. Fluids Struct.* **10** (5), 439–453.

NEWMAN, D. J. & KARNIADAKIS, G. E. 1997 A direct numerical simulation study of flow past a freely vibrating cable. *J. Fluid Mech.* **344**, 95–136.

RAGHAVAN, K. & BERNITSAS, M. M. 2011 Experimental investigation of Reynolds number effect on vortex induced vibration of rigid circular cylinder on elastic supports. *Ocean Engng* **38** (5-6), 719–731.

ROVERI, F. E. & VANDIVER, J. K. 2001 SlenderEx: using SHEAR7 for assessment of fatigue damage caused by current induced vibrations. In *Proceedings of the 20th OMAE Conference*, pp. 3–8. American Society of Mechanical Engineers.

SARPKAYA, T. 1978 Fluid forces on oscillating cylinders. *NASA STI/Recon Tech. Rep.* A **78**, 275–290.

SARPKAYA, T. 1995 Hydrodynamic damping, flow-induced oscillations, and biharmonic response. *J. Offshore Mech. Arctic Engng* **117** (4), 232–238.

SARPKAYA, T. 2004 A critical review of the intrinsic nature of vortex-induced vibrations. *J. Fluids Struct.* **19** (4), 389–447.

STAUBLI, T. 1983 *Untersuchung der oszillierenden Kräfte am querangeströmten, schwingenden Kreiszylinder*. ETH Zurich.

TANG, G., LU, L., TENG, B., PARK, H., SONG, J. & ZHANG, J. 2011 Identification of hydrodynamic coefficients from experiment of vortex-induced vibration of slender riser model. *Sci. China Tech. Sci.* **54** (7), 1894–1905.

TECHET, A. H., HOVER, F. S. & TRIANTAFYLLOU, M. S. 1998 Vortical patterns behind a tapered cylinder oscillating transversely to a uniform flow. *J. Fluid Mech.* **363**, 79–96.

THOMPSON, M., HOURIGAN, K. & SHERIDAN, J. 1996 Three-dimensional instabilities in the wake of a circular cylinder. *Exp. Therm. Fluid Sci.* **12** (2), 190–196.

TRIANTAFYLLOU, M. S., TRIANTAFYLLOU, G. S., TEIN, Y. S. & AMBROSE, B. D. 1999 Pragmatic riser VIV analysis. In *Offshore Technology Conference*. Offshore Technology Conference.

VANDIVER, J. K., JAISWAL, V. & JHINGRAN, V. 2009 Insights on vortex-induced, traveling waves on long risers. *J. Fluids Struct.* **25** (4), 641–653.

VANDIVER, J. K., SWITHENBANK, S. B., JAISWAL, V. & JHINGRAN, V. 2006 Fatigue damage from high mode number vortex-induced vibration. In *Proceedings of the 25th OMAE Conference*, pp. 803–811. American Society of Mechanical Engineers.

VIOLETTE, R., DE LANGRE, E. & SZYDLOWSKI, J. 2007 Computation of vortex-induced vibrations of long structures using a wake oscillator model: comparison with DNS and experiments. *Comput. Struct.* **85** (11–14), 1134–1141.

WANG, X., SO, R. & CHAN, K. 2003 A non-linear fluid force model for vortex-induced vibration of an elastic cylinder. *J. Sound Vib.* **260** (2), 287–305.

WANG, Z., TRIANTAFYLLOU, M. S., CONSTANTINIDES, Y. & KARNIADAKIS, G. M. 2018 A spectral-element/Fourier smoothed profile method for large-eddy simulations of complex VIV problems. *Comput. Fluids* **172**, 84–96.

WANG, Z., TRIANTAFYLLOU, M. S., CONSTANTINIDES, Y. & KARNIADAKIS, G. M. 2019 An entropy-viscosity large eddy simulation study of turbulent flow in a flexible pipe. *J. Fluid Mech.* **859**, 691–730.

WILLIAMSON, C. H. K. 1996 Vortex dynamics in the cylinder wake. *Annu. Rev. Fluid Mech.* **28** (1), 477–539.

WILLIAMSON, C. H. K. & GOVARDHAN, R. 2004 Vortex-induced vibrations. *Annu. Rev. Fluid Mech.* **36**, 413–455.

WILLIAMSON, C. H. K. & GOVARDHAN, R. 2008 A brief review of recent results in vortex-induced vibrations. *J. Wind Engng Ind. Aerodyn.* **96** (6–7), 713–735.

WILLIAMSON, C. H. K. & ROSHKO, A. 1988 Vortex formation in the wake of an oscillating cylinder. *J. Fluids Struct.* **2** (4), 355–381.

WU, J. 2011 Hydrodynamic force identification from stochastic vortex induced vibration experiments with slender beams. PhD thesis, Norwegian University of Science and Technology.

WU, J., SHERIDAN, J., WELSH, M. C. & HOURIGAN, K. 1996 Three-dimensional vortex structures in a cylinder wake. *J. Fluid Mech.* **312**, 201–222.

ZHENG, H., DAHL, J. M., MODARRES-SADEGHI, Y. & TRIANTAFYLLOU, M. S. 2014*a* Coupled inline-cross flow vortex-induced vibration hydrodynamic coefficients database. In *ASME 2014 33th International Conference on Ocean, Offshore and Arctic Engeering,* p. V002T08A087. American Society of Mechanical Engineers.

ZHENG, H., PRICE, R. E., MODARRES-SADEGHI, Y. & TRIANTAFYLLOU, M. S. 2014*b* On fatigue damage of long flexible cylinders due to the higher harmonic force components and chaotic vortex-induced vibrations. *Ocean Engng* **88**, 318–329.